LITHOS 458-459 (2023) 107344

Contents lists available at ScienceDirect

LITHOS

journal homepage: www.elsevier.com/locate/lithos

# Concurrent adakitic and non-adakitic Late Miocene-Quaternary magmatism at the Sahand volcano, Urumieh-Dokhtar Magmatic Arc (NW Iran)

Lorenzo Fedele [a,*], Javad Mehdipour Ghazi [b], Samuele Agostini [c], Sara Ronca [d], Francesca Innocenzi [c,d], Michele Lustrino [d,e]

[a] Dipartimento di Scienze della Terra, dell'Ambiente e delle Risorse (DiSTAR), Università degli Studi di Napoli Federico II, Via Vicinale Cupa Cintia 21, 80126 Napoli, Italy
[b] Shahid Beheshti University, Shahid Shahriari Square, Daneshjou Boulevard, Shahid Chamran Highway, Tehran, Iran
[c] CNR - Istituto di Geoscienze e Georisorse, Sede Principale di Pisa, Via G. Moruzzi 1, 56124 Pisa, Italy
[d] Dipartimento di Scienze della Terra, Sapienza Università di Roma, P.le A. Moro 5, 00185 Roma, Italy
[e] CNR - Istituto di Geologia Ambientale e Geoingegneria c/o Dipartimento di Scienze della Terra, Sapienza Università di Roma, P.le A. Moro 5, 00185 Roma, Italy

ARTICLE INFO

*Keywords:*
Urumieh-Dokhtar
Continental collision
Subduction-related
Adakite
Calcalkaline

ABSTRACT

The Sahand volcano in NW Iran is characterised by voluminous Late Miocene to Quaternary magmatic activity. Petrographic, mineral chemical, whole-rock geochemical and Sr-Nd-Pb isotope data allowed to identify two rock groups, continuously emplaced from the ancient Paleo-Sahand to the later Neo-Sahand stages. These are represented by abundant evolved rocks, with dacitic to rhyolitic compositions and less common intermediate (andesitic) rocks. Both rock types have the typical LILE-enriched and HFSE-depleted fingerprints of magmas originated from subduction-modified mantle sources, as well as radiogenic Sr- and Pb- (18.8–18.9 $^{206}Pb/^{204}Pb$, 15.6–15.7 $^{207}Pb/^{204}Pb$ and 38.8–39.2 $^{208}Pb/^{204}Pb$) isotope compositions. Nevertheless, the evolved rocks have lower $^{87}Sr/^{86}Sr$ (0.70437–0.70491 vs 0.70494–0.70585) and display an evident high Sr/Y vs Y and high La/Yb vs Yb "adakitic" signature, suggesting derivation from the partial melting of lower continental crust rocks, rather than from the differentiation of the non-adakitic intermediate rocks. The latter would be the derivative melts of magmas generated by the partial melting of lithospheric mantle sources modified by metasomatic fluids released by the subducted Neotethyan oceanic lithosphere. During their ascent and differentiation, these magmas likely provided the heat necessary to induce partial melting of the lower continental crust, eventually producing adakitic evolved magmas. Quantitative models and geothermobarometric calculations suggest that differentiation processes for both rock groups occurred mainly by polybaric fractional crystallisation (in the 29–4 km depth range), possibly coupled with minor assimilation of local crustal rocks.

The peculiar style of the Sahand magmatic activity (with both adakitic and non-adakitic products) and its temporal evolution (with an overall increase of the degree of evolution and a decrease of the non-adakitic melts) are somewhat different with respect to those of the coeval neighbouring districts of Saray, Sabalan and Bijar-Qorveh. These can be reconciled within a general model for NW Iran where magmatism is triggered by upwelling of the sub-lithospheric mantle as a consequence of slab break-off (or the opening of a slab tear). The progressive propagation (and subsequent exhaustion) of the thermal pulse and the increasing thickness of the continental crust played a main role in determining both the progressively later inception of active magmatism (from ~11 to 4.5 Ma) and the change in magma types (from largely variable to adakitic only) at increasing distance from the Iran-Arabia suture.

## 1. Introduction

Iran is an outstanding natural laboratory for investigating the entire range of processes that shape the continental and oceanic crust, including formation, accretion, subduction of oceanic plates and a wide range of soft to hard collisional tectonics (e.g., Stern et al., 2021). These processes are also associated to the formation of ore deposits of strategically relevant metals in connection with Late Proterozoic to Cenozoic

* Corresponding author.
*E-mail address:* lofedele@unina.it (L. Fedele).

https://doi.org/10.1016/j.lithos.2023.107344
Received 22 June 2023; Received in revised form 1 September 2023; Accepted 2 September 2023
Available online 6 September 2023

tectono-magmatic phases (e.g., Rabiee et al., 2022). The long geological evolution recorded in basement rocks testifies a complex history of oceanic spreading phases followed by island-arc magmatism, back-arc opening and continental drifting (e.g., Muttoni et al., 2009; Shafaii Moghadam et al., 2020; Stern et al., 2021). Additional, more accessible sources of information lie within the rock successions emplaced during Mesozoic-Cenozoic times, witnessing evolution from a passive continental margin, to an extremely active Andean-type magmatic arc system and eventually to the present-day continental orogen setting (e.g., van Hinsbergen et al., 2020).

In such a context, the northwesternmost part of Iran can be regarded as a remarkable key-area, as many of the main tectonomagmatic events that characterised the Cenozoic evolution of Iran and Lesser Caucasus are documented in the local geological record (e.g., Rabiee et al., 2022). The magmatic activity in NW Iran includes products mostly related to the Mesozoic Sanandaj-Sirjan Zone magmatic belt, the Cenozoic Urumieh-Dokhtar Magmatic Arc, and the Lesser Caucasus and Alborz magmatic districts. The Cenozoic activity in NW Iran essentially indicates derivation of magmas from subduction-modified mantle sources, both in the context of back-arc tectonics and active collisional setting. During the end of the Cenozoic, the chemical compositions of the emplaced products widened to include Miocene potassic to ultrapotassic and adakitic compositions, as well as the products of a Pliocene-Quaternary intraplate-like magmatic cycle, the latter still bearing evidence of some contribution from subduction-modified mantle components (e.g., Fedele et al., 2022; Lustrino et al., 2021). Therefore, the study of magmatism in NW Iran offers a unique opportunity to investigate all such processes, to elucidate the possible temporal variations in terms of local geotectonic evolution or as inheritance of past modification processes of the mantle sources, unrelated to coeval tectonics.

In this paper, we present a full set of petrographic, mineral chemical and whole-rock geochemical (major oxides, trace element and Sr-Nd-Pb isotope ratios) data for the Late Miocene to Quaternary magmatic rocks of the Sahand volcano, one of the largest edifices of NW Iran. Our purpose is to contribute to shed light on the complex collisional magmatism that characterised the area, and to provide fruitful clues to unravelling the related geodynamic processes.

## 2. Geological background

### 2.1. Regional geology

The nucleus of Iran continental crust was assembled in Ediacaran-Paleozoic times as a sector of a ~5000 km-long continental magmatic arc developed along the northern margin of the Greater Gondwana (or Pannotia) continent (e.g., Stern et al., 2021). During Late Permian-Late Triassic, part of this magmatic arc peeled off from the north-western Gondwana margin, which lead to the opening the Neotethys Ocean, and then collided with the southern margin of Eurasia, closing the Paleotethys Ocean (e.g., Alavi, 1994; Şengör et al., 2023; Verdel et al., 2011). The thinned and weakened southwestern passive margin of Iran became the site of a new NE-directed subduction of the young Neotethyan oceanic lithosphere (e.g., van Hinsbergen et al., 2020). This led to the development of the Mesozoic Sanandaj-Sirjan Zone (SSZ), a ~150 km wide magmatic belt running NW-SE for ~1500 km along SW Iran (e.g., Deevsalar et al., 2017; Hassanzadeh and Wernicke, 2016).

The SSZ consists of large gabbroic and granitoid plutons with subduction-related calcalkaline fingerprint, intruding a basement of Late Proterozoic-Mesozoic metamorphic rocks (mostly gneiss and amphibolite), overlain by Mesozoic shallow-water sediments of the former passive continental margin (e.g., Chiu et al., 2013; Hassanzadeh and Wernicke, 2016; Mehdipour Ghazi and Moazzen, 2015; Rahimzadeh et al., 2021). According to recent alternative models, magmatism in the district developed within a context of continental rift, mostly based on the observed migration with time of active magmatism towards the NW (from ~175 to ~145 Ma; Hunziker et al., 2015; Azizi and Stern, 2019). In this view, the "arc-like" subduction-related signature would be acquired by means of a significant crustal contamination of mantle-derived magmas.

Calcalkaline magmatism in the SSZ progressively shifted towards NE, leading to the development of the sub-parallel Urumieh-Dokhtar Magmatic Arc (UDMA), whose earliest phases of activity range from late Cretaceous to Paleogene (e.g., Hassanzadeh and Wernicke, 2016; Rabiee et al., 2020). The development of UDMA is generally interpreted as reflecting the flattening of the Neotethyan subduction angle (e.g., Chiu et al., 2013; Verdel et al., 2011). Additional magmatism related to collision of Arabia is recorded in the Lesser Caucasus and Alborz districts (northern Iran), generally ascribed to a back-arc setting (e.g., Asiabanha and Foden, 2012; Moghadam et al., 2018), in Central Iran and in the Lut-Sistan areas (easternmost Iran; e.g., Pang et al., 2013a), and in the Makran arc of SE Iran, where N-directed subduction of the oceanic lithosphere was considered active from ~7.5 to ~0.8 Ma (e.g., Delavari et al., 2022). The continued subduction of the Neotethyan slab along UDMA eventually reached a stage of diachronous continental collision between the Arabian and Iranian plates (e.g., Alavi, 1994; Chiu et al., 2013; Pang et al., 2016). This resulted in the progressive thickening and shortening of the continental crust (e.g., Hassanzadeh and Wernicke, 2016) and in the formation of the Bitlis-Zagros Orogen, from Anatolia (Bitlis) to Iran (Zagros; e.g., McQuarrie and van Hinsbergen, 2013).

The peak of activity in the UDMA occurred during the so-called Eocene flare-up, when abundant calcalkaline magmas (plus rarer tholeiitic and transitional shoshonitic melts) with subduction-related geochemical signature were emplaced in a context of lithospheric back-arc extension (e.g., Omrani et al., 2008; Rabiee et al., 2020; Verdel et al., 2011). A significant decrease in intensity was then recorded after the attainment of continental collision (in late Eocene-Oligocene times), which eventually led to a progressive cessation of any igneous activity from NW to SE (e.g., Chiu et al., 2013). This stage was accompanied by the post-collisional emplacement of additional subduction-related rock types, including ultrapotassic (Ahmadzadeh et al., 2010; Lustrino et al., 2019; Pang et al., 2013b) and adakitic rocks (e.g., Fedele et al., 2022; Jahangiri, 2007; Omrani et al., 2008; Salari et al., 2021). Emplacement of more sporadic intraplate-like alkaline rocks akin to those coevally emplaced in SE Anatolia and Lesser Caucasus (e.g., Ahmadzadeh et al., 2010; Allen et al., 2013; Fedele et al., 2022; Jahangiri, 2007; Kheirkhah et al., 2009; Lustrino et al., 2012; Neill et al., 2015; Omrani et al., 2008; Verdel et al., 2011) is also reported. Recently, low-volume outcrops of ultrabasic-ultracalcic melanephelinite-melilitite rocks were also found in northern UDMA (Lustrino et al., 2021).

### 2.2. The Sahand volcano

The Sahand volcano, in NW UDMA (Fig. 1), is a polyphase Miocene-Quaternary stratovolcano producing pyroclastic deposits, lava flows and domes, mostly of intermediate to evolved compositions. The volcano lies on a basement consisting of Paleozoic-Mesozoic sedimentary deposits, Eocene volcanic rocks, marls of the Lower Miocene Qom Formation, and Middle-to-Late Miocene marls, sandstones and gypsum red beds of the Upper Red Formation (e.g., Abbassi et al., 2021). Along with the neighbouring Saray and Sabalan edifices, the Sahand volcano forms a rough array at increasing distances from the present-day Neotethyan suture.

According to Moine Vaziri and Amine Sobhani (1977), the volcanic activity at Sahand can be subdivided into three periods: 1) ~12–9 Ma, with emplacement of calcalkaline basaltic andesites and andesites, cropping out mainly in the western part; 2) ~10–5 Ma, with calcalkaline dacitic and minor andesitic magmas diffusely occurring as tuff and ignimbrite deposits; 3) a final Quaternary stage of andesitic and dacitic activity. The oldest products of the Sahand activity are represented by the thick pyroclastic sequence of the GermeziGol Formation, cropping out on the western flank of the volcano (Moine Vaziri and Amine Sobhani, 1977). These were first K—Ar dated at ~12 Ma by Moine Vaziri

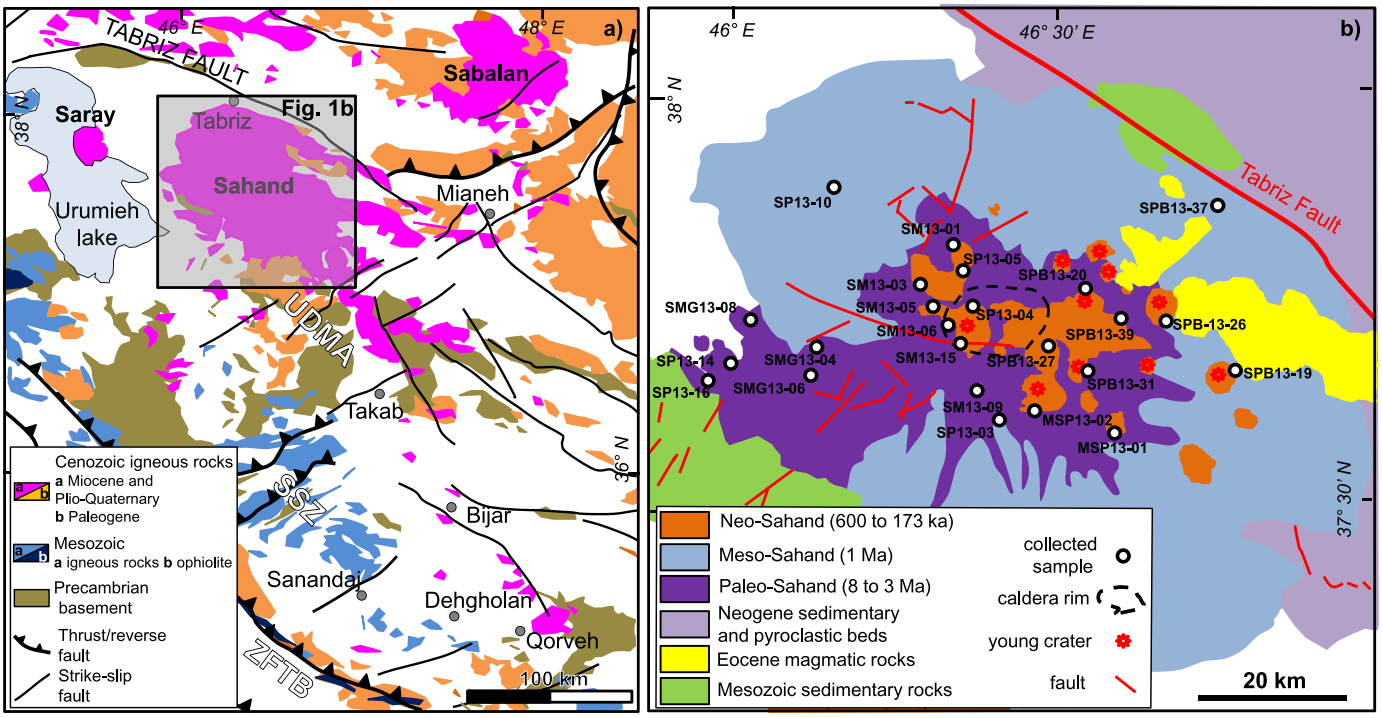


**Fig. 1.** a) Simplified geological map of NW Iran (SSZ Sanandaj-SirjanZone, UDMA Urumieh-Dokhtar Magmatic Arc; modified after Rabiee et al., 2020), with grey rectangle highlighting the investigated area. b) Geological sketch map of the Sahand volcano (after Ghalamghash et al., 2019).

and Amine Sobhani (1977), but more recent radiometric data of some underlying stratigraphic units significantly questioned this estimate, yielding ages of 11.6–10 Ma for Lignite Beds and 10–7.5 Ma for Fish beds (apatite and zircon fission tracks; Reichenbacher et al., 2011), and 8.66–7.42 Ma to 8.14–6.96 Ma for some intercalated pumice beds ($^{40}Ar/^{39}Ar$ and K—Ar methods; Swisher, 1996; Sawada et al., 2016). The few available age data on Sahand products were obtained by zircon U—Pb in more recent times by Chiu et al. (2013) and Lechmann et al. (2018). The first authors report ages of 6.5, 5.8 and 5.3 Ma, while the second dated four samples from domes cropping out on the western flank of the volcano between 5.64 and 5.34 Ma.

Based on a revision of the above literature and on 12 new U—Pb and U—Th zircon ages (7.83–0.194 Ma), Ghalamghash et al. (2019) proposed a new subdivision of Sahand volcanism in three phases: Paleo-Sahand (8–3 Ma), Meso-Sahand (~1 Ma) and Neo-Sahand (~0.6–0.2 Ma). During the Paleo-Sahand period, the ancient stratovolcano was built through the emplacement of both lava and pyroclastic deposits. The successive Meso-Sahand stage was characterised by the emplacement of flat-lying ignimbrite deposits, which spread over the entire edifice area. This period culminated with a volcanic collapse and the formation of a caldera, after which the latest Neo-Sahand stage shortly followed. The products of this recent volcanism are represented by numerous domes and parasitic scoria cones, typically of limited areal extent (5–15 $km^2$).

The igneous products of the Sahand volcano have been ascribed to low melting degrees (1–5%) of a subduction-modified, garnet- and spinel-bearing peridotite lithospheric source (plus subsequent crustal differentiation via assimilation and fractional crystallisation AFC processes), triggered by the asthenospheric upwelling caused by the break-off of the subducted Neothethyan oceanic slab (Ghalamghash et al., 2019). Sinking to the NE of the detached slab would have also resulted in the SW to NE age progression of active volcanism along the Saray-Sahand-Sabalan volcanic array. The larger crustal thickness attained beneath the Sabalan volcano has been invoked to explain the $K_2O$- and incompatible elements-richer composition of the Sabalan magmas with respect to those of the Sahand (Ghalamghash et al., 2019). The occurrence of andesitic-dacitic-rhyolitic rocks with a clear adakitic geochemical fingerprint is also reported for the Sahand, their genesis being ascribed to partial melting of a delaminated garnet-bearing lower crustal source (possibly represented by high-pressure cumulates; Lechmann et al., 2018), which was activated after the Iran-Arabia continental collision (Pirmohammadi Alishah and Jahangiri, 2013).

## 3. Materials and methods

Sixty-two samples were collected from the entire extension of the Sahand volcano. The rocks were ascribed to the Paleo-Sahand and Neo-Sahand periods of activity, following the geochronological scheme of Ghalamghash et al. (2019), as indicated in Fig. 1. In this map, two samples fall in the field for the Meso-Sahand deposits, but these were actually collected from a lava body lying below the Meso-Sahand pyroclastic deposits (SP13–10, thus ascribed to the Paleo-Sahand stage) and from a granitoid body cropping out at the NE edge of the volcano apron, presumably Eocene in age (SP13–37).

The freshest 24 samples were prepared for petrographic and whole-rock geochemical characterisation. Twelve representative samples (in terms of periods of activity and lithotypes, as described below) were selected for EPMA (Electron Probe Micro Analyzer) characterisation of the main mineral and glass phases and eleven of them were also analysed for Sr-Nd-Pb isotopes. Full analytical and procedural details are reported in the Supplementary material 1. Full results, sampling locations and quality control data are reported in the Supplementary material 2 as Tables S2.1–13.

## 4. Results

### 4.1. Petrography

Two main lithotypes are recognised among the investigated samples. A first group includes rocks with plagioclase and pyroxenes as the main phases, thus ascribed to an "intermediate" rock type. The second group is represented by an "evolved" rock type where plagioclase is the

dominating phase, generally associated with less abundant amphibole and biotite.

Rocks of the intermediate group are relatively rare and more represented in the samples belonging to the oldest, Paleo-Sahand period of activity. These display a seriate, moderately porphyritic to glomeroporphyritic texture (occasionally weakly vesicular; e.g., sample SMG13–08) with a very fine-grained hypocrystalline groundmass (Fig. 2a). The dominant phenocryst phase is plagioclase, followed by orthopyroxene, clinopyroxene and fewer opaque minerals (mainly as microphenocrysts), in decreasing order of abundance. Few, small olivine microphenocrysts, generally rounded, resorbed and completely replaced by iddingsite, are also observed in samples SMG13–04 and SMG13–08. The occasional presence of brown-green amphibole phenocrysts is observed for sample SP13–06. The groundmass is made of the same mineral phases and glass (relatively abundant in sample SP13–06).

Intermediate rocks from the Neo-Sahand activity show a variably altered, seriate, strongly to moderately porphyritic/glomeroporphyritic texture (occasionally weakly vesicular), with a hypocrystalline to holocrystalline groundmass (Fig. 2b). Phenocrysts are mainly plagioclase (up to 0.8 mm in length and generally with sieve-textured cores), orthopyroxene, clinopyroxene and opaques. Some samples also display sparse phenocrysts of brown amphibole with opacitised rims (samples SP13–26, SPB 13–27 and SPB13–39), biotite (SP13–26) or apatite microphenocrysts (SPB13–27 and SPB13–39). The ferromagnesian minerals are variably replaced by aggregates of chlorite, green amphibole and epidote. The intergranular to intersertal groundmass is made of plagioclase, clinopyroxene, orthopyroxene, opaques and apatite, and includes diffuse intergranular alkali feldspar. Glass is generally scarce and devitrified. Some secondary/hydrothermal quartz is also present. Some quartzitic xenoliths, consisting mainly of deformed quartz aggregates (samples SP13–27 and SP13–39; Fig. 2c) and resorbed quartz with plagioclase + orthopyroxene + clinopyroxene corona (SP13–26) were also recognised.

Rocks of the evolved group are extremely abundant, especially in the products of the Neo-Sahand period. No significant differences have been observed between older and younger samples of this group. The rocks are characterised by a seriate, moderately to strongly porphyritic/glomeroporphyritic texture (with about 25–30 vol% of phenocrysts/glomerocrysts) and a hypocrystalline to hypohyaline groundmass (Fig. 2d,e). Plagioclase is the dominant phenocryst phase, typically up to 5–6 mm in length, often found in both mono- and polymineralic glomerocrysts, and commonly showing sieve-textured cores. Less abundant phenocryst phases include reddish-brown to brown amphibole, orthopyroxene, clinopyroxene, subordinate biotite (often rimmed by amphibole) and opaque minerals. Amphibole is generally the main ferromagnesian phase, except for a few samples where orthopyroxene (Paleo-Sahand SP13–10 and Neo-Sahand SPB13–19, SM13–06, SM13–15 and SP13–05) or biotite (SM13–05, Neo-Sahand) prevail. Rounded resorbed quartz phenocrysts are also observed in several Neo-Sahand samples (SM13–03, SM13–05, SM13–06, SM13–09 and SP13–04). Glomerocrysts made of amphibole + plagioclase + biotite ± opaques ± quartz are diffuse in all the samples. Groundmass is

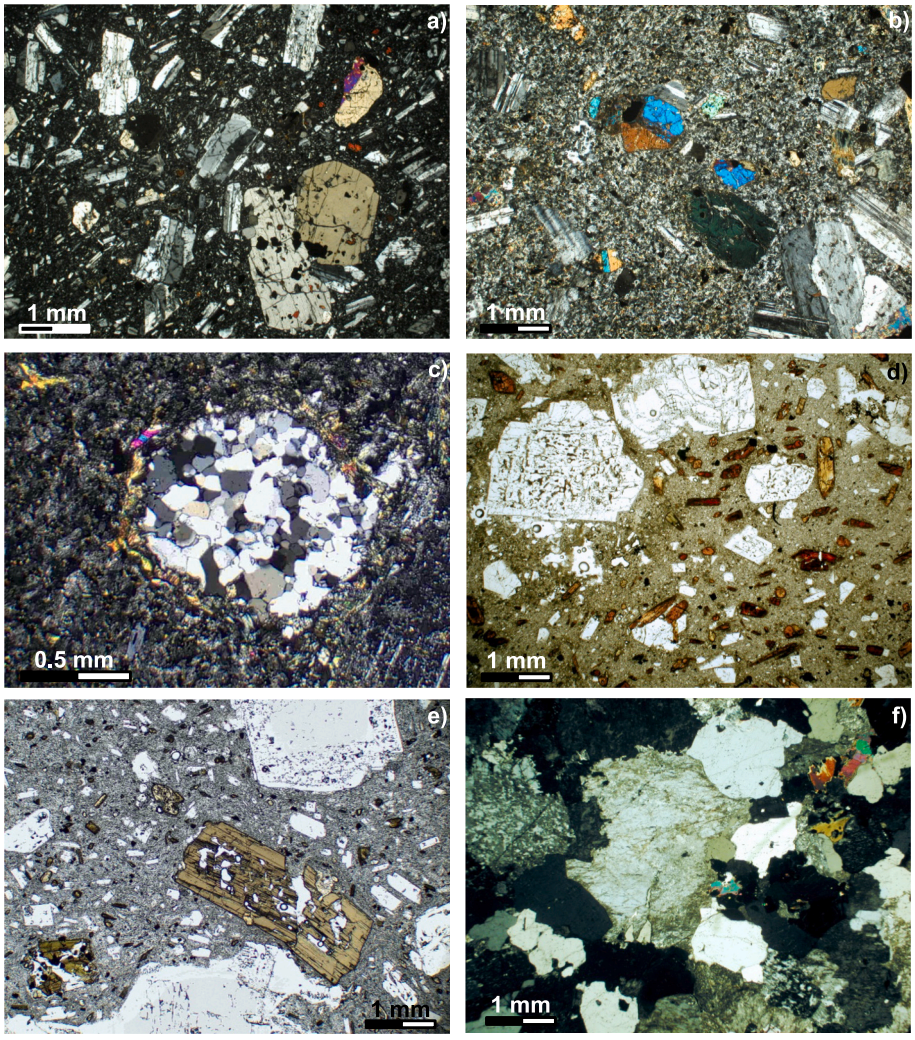


**Fig. 2.** Representative photomicrographs of the investigated rock samples from the Sahand volcano. a) Paleo-Sahand intermediate sample SMG13–04 (crossed polarisers light view, CP) showing a moderately porphyritic/glomeroporphyritic texture with phenocrysts of plagioclase, orthopyroxene (lower right) and clinopyroxene (e.g. upper right) and small iddingsitised olivine microlites (reddish) set into a hypocrystalline groundmass; b) Neo-Sahand intermediate sample SPB13–20 (CP) showing a moderately porphyritic texture with phenocrysts of plagioclase, clinopyroxene and orthopyroxene (e.g. upper right) set into a holocrystalline groundmass; c) Neo-Sahand intermediate sample SPB13–27 (CP) showing a clinopyroxene-rimmed quartzitic xenolith; d) Paleo-Sahand evolved sample SP13–14 and e) Neo-Sahand evolved sample SPB13–15 (plane polarised light view, PP) showing a moderately porphyritic textures with plagioclase and amphibole phenocrysts set into a hypocrystalline groundmass; f) granitoid sample SPB13–37 (CP) showing a autoallotriomorphic texture with grains of alkali feldspar (dusty), quartz (limpid) and biotite (high interference colours, e.g. upper right).

microcrystalline to hypohyaline and consists of plagioclase, orthopyroxene, brown amphibole, opaques and variable amounts of glass. Intergranular alkali feldspar crystals were found in some Neo-Sahand samples featuring lesser glass (SM13–09, SP13–05 and MSP13–01). Diffuse secondary carbonate phases have been observed in the groundmass of two Neo-Sahand samples (SP13–03 and SP13–04).

The single sample collected from a granitoid body (SPB13–37) displays a fine/medium-grained holocrystalline autoallotriomorphic texture and a leucocratic paragenesis (Fig. 2f). The main mineral phases include large perthitic alkali feldspar crystals, quartz, plagioclase, rare biotite and accessory opaque, apatite and zircon.

### 4.2. Mineral chemistry

#### 4.2.1. Plagioclase

Plagioclase is ubiquitous in all the investigated rocks. Paleo-Sahand intermediate samples include the Ca-richest bytownite-labradorite compositions, with a somewhat progressive decrease of Ca contents from phenocryst cores ($Ab_{20-39}An_{59-79}Or_{1}$) to phenocryst rims ($Ab_{28-42}An_{55-71}Or_{1}$) up to groundmass microlites ($Ab_{30-46}An_{52-68}Or_{1-2}$; Fig. 3a). Neo-Sahand intermediate samples are characterised by generally Ca-poorer and K-richer labradorite-andesine compositions, with largely overlapping ranges for crystal cores ($Ab_{37-66}An_{30-62}Or_{1-4}$), rims ($Ab_{37-57}An_{32-65}Or_{1-3}$ plus one unusually K-rich analysis with $Or_{11}$) and groundmass crystals ($Ab_{39-61}An_{31-60}Or_{1-4}$ plus one crystal with $Or_{9}$). The evolved samples feature mostly andesine (plus fewer labradorite), with Paleo-Sahand rocks showing a narrower compositional range ($Ab_{50-63}An_{32-49}Or_{1-3}$) with respect to Neo-Sahand ones ($Ab_{44-67}An_{31-56}Or_{1-3}$ plus one sample with oligoclase microlites). Plagioclase crystals from the granitoid sample are remarkably homogeneous, Na-rich oligoclase ($Ab_{80-82}An_{15-17}Or_{10-12}$).

#### 4.2.2. Alkali feldspar

The relatively abundant alkali feldspar microlites found in the groundmass of Neo-Sahand intermediate samples cover a large compositional range ($Ab_{20-46}An_{2-6}Or_{42-79}$ plus one K-rich crystal with $Or_{92}$; Fig. 3a). Crystals from the granitoid sample are more homogeneous and Na-richer ($Ab_{47-59}An_{2-3}Or_{38-51}$ plus a single K-richer $Ab_{28}An_{1}Or_{71}$ composition).

#### 4.2.3. Olivine

Few fresh olivine crystals were found in the groundmass of Paleo-Sahand intermediate samples, with $Fo_{58-62}$. The sporadic microphenocrysts are mostly pseudomorphosed by iddingsite, and thus were not analysed.

#### 4.2.4. Clinopyroxene

Clinopyroxenes from both Paleo- and Neo-Sahand intermediate samples display a relatively homogeneous augite composition (respectively $En_{40-44}Wo_{40-43}Fs_{14-19}$ and $En_{40-45}Wo_{40-44}Fs_{13-20}$; Fig. 3b), some belonging to the aluminian type (i.e. with Al > 0.1 apfu, based on six oxygens). No systematic difference was observed between crystal cores, crystal rims and groundmass microlites. Some pigeonite microlites ($En_{50-57}Wo_{8-10}Fs_{33-40}$) were also found in Paleo-Sahand intermediate samples. In the Neo-Sahand intermediate sample SPB13–26, clinopyroxene crystals forming a corona around a large quartz xenocryst are Si-richer (1.992–1.999 apfu) and Al-poorer (0.010–0.021) compared to the bulk of clinopyroxene analyses (1.856–1.936 apfu and 0.061–0.136 apfu for Si and Al, respectively).

#### 4.2.5. Orthopyroxene

A relatively large spectrum of orthopyroxene compositions was observed in the Paleo-Sahand intermediate rocks, covering the $En_{60-69}Wo_{1-5}Fs_{27-35}$ range (with a rough decrease of Mg contents from core to rim and groundmass). Intermediate Neo-Sahand samples are more homogeneous and Mg-richer ($En_{72-74}Wo_{2-3}Fs_{22-26}$). Finally, orthopyroxene

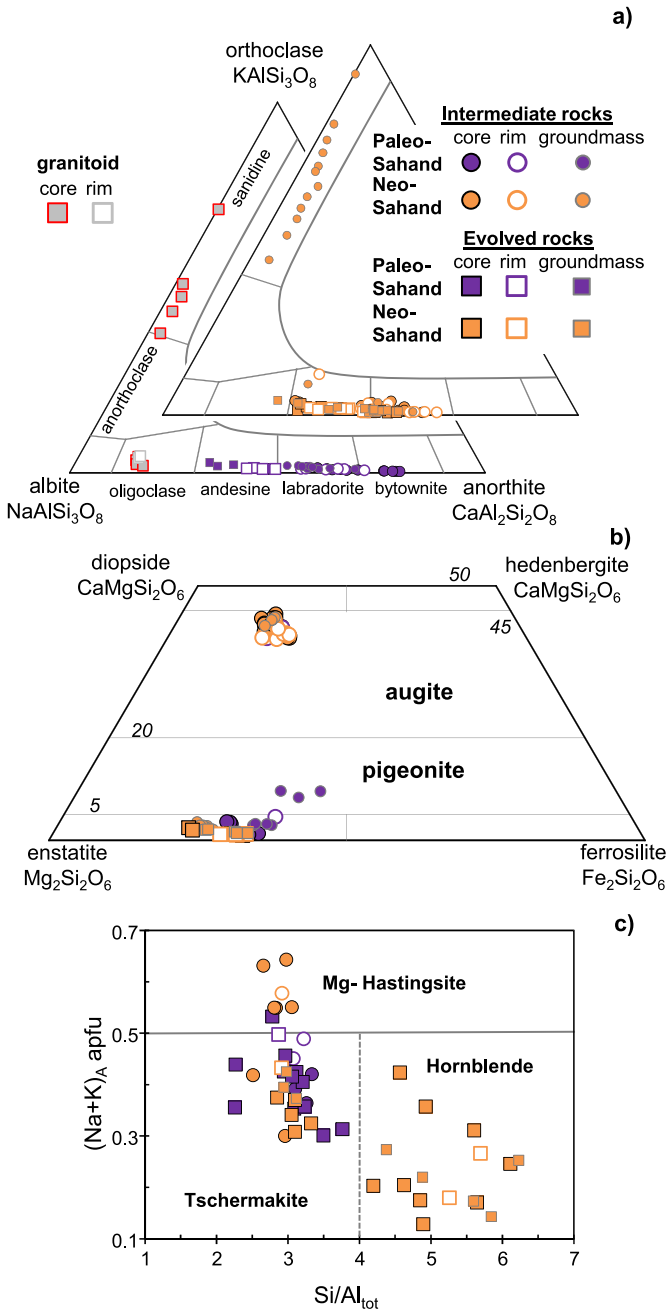


**Fig. 3.** Classification of the analysed a) feldspar and b) pyroxene crystals and c) $(Na + K)_A$ vs $Si/Al_{tot}$ diagram for amphibole crystals of the investigated rock samples from the Sahand volcano.

crystals from Neo-Sahand evolved samples span the $En_{67-76}Wo_{1-2}Fs_{25-32}$ range and show no systematic difference between different data points.

#### 4.2.6. Amphibole

Amphibole crystals belong to the calcic-group ($Ca_B \geq 1.50$ apfu, based on 24 oxygens), mostly classifying as magnesio-hornblende/tschermakite/tschermakitic hornblende [$(Na + K)_A < 0.50$ apfu], plus few magnesio-hastingsite [$(Na + K)_A \geq 0.50$ apfu, $^{VI}Al < Fe^{3+}$] in some intermediate Neo-Sahand and evolved Paleo-Sahand samples (Fig. 3c). In the Paleo- and Neo-Sahand intermediate rocks crystals are generally homogeneous in composition, with $Si/Al_{tot}$ of 3.07–3.33 and 2.51–3.05, and Na of 0.569–0.639 and 0.645–0.741 apfu, respectively. Similar compositions were observed in the Paleo-Sahand evolved rocks, though covering a larger spectrum ($Si/Al_{tot}$ 2.26–3.77, Na 0.514–0.671 apfu,

plus one with 0.837 apfu of Na). The Neo-Sahand evolved rocks include amphibole crystals similar to those described above ($Si/Al_{tot}$ 2.85–3.32, Na 0.591–0.655 apfu) but also a more abundant Si-richer and Al- and Na-poorer variety ($Si/Al_{tot}$ 4.20–6.23, Na 0.349–0.521 apfu).

#### 4.2.7. Biotite

Trioctahedral biotite mica was analysed only in the evolved samples, with a striking compositional variability between Paleo-Sahand (Fe-richer; Fe 2.097–2.281, Ti 0.303–0.318, Mg 2.593–2.750 apfu) and Neo-Sahand rocks (Ti- and Mg-richer; Fe 1.400–1.992, Ti 0.326–0.405, Mg 2.994–3.503 apfu; Supplementary material 2). Biotite from the granitoid sample is remarkably richer in Mg (3.726–4.062 apfu), K (1.864–1.921 vs 1.639–1.777 apfu for Paleo- and Neo-Sahand rocks) and F (> 4.19 vs. < 1.02 wt%), and poorer in Ti (0.169–0.204 apfu) and Al (1.901–2.269 vs 2.521–2.862 apfu).

#### 4.2.8. Opaque minerals

Most of these phases belong to the magnetite-ulvöspinel solid solution. Crystals from Paleo-Sahand rocks are overall homogeneous in composition, both in the intermediate (Usp 24–36 mol%) and in the evolved rocks (Usp 1.3–7.9 mol%; Supplementary material 2). Opaque minerals form Neo-Sahand rocks are more variable in composition, covering the 7–53 (in intermediate rock types) and 2–83 Usp mol.% (evolved rocks) ranges, and including few Ti-richer microlites falling in the ilmenite-hematite rhombohedral phase solid solution.

#### 4.2.9. Apatite and glass

Few apatite crystals were analysed in the Neo-Sahand intermediate and evolved rocks, showing no systematic differences except for higher F in the first rock type (2.68–2.82 vs 1.54–1.67 wt%). Fresh glass was found mainly in the groundmass of Neo-Sahand evolved rocks, yielding extremely evolved rhyolitic compositions ($SiO_2$ = 77.6–79.7 wt%, $Na_2O + K_2O$ = 7.26–8.72 wt%). Some slightly $SiO_2$-poorer and FeO-richer rhyolitic glass was analysed in the groundmass of a Paleo-Sahand intermediate sample and as inclusions in plagioclase crystals from a Paleo-Sahand evolved sample (Supplementary material 2).

### 4.3. Whole-rock geochemistry

The whole-rock composition of the investigated rock samples from the Sahand volcano (Table S2.12 in the Supplementary material 2) was compared with existing literature data and with the products of the nearly coeval neighbouring edifices of the Saray (or "Eslamieh Peninsula", ~11 Ma; Moayyed et al., 2008; Pang et al., 2013b; Moghadam et al., 2014) and Sabalan (subdivided into Paleo-Sabalan and Neo-Sabalan stages, ranging from 4.5 to 1.3 Ma and from 545 to 149 ka, respectively; Ghalamghash et al., 2016). Additional comparisons were made with the Miocene (11.7–8 Ma) "adakitic" dacitic rocks from the

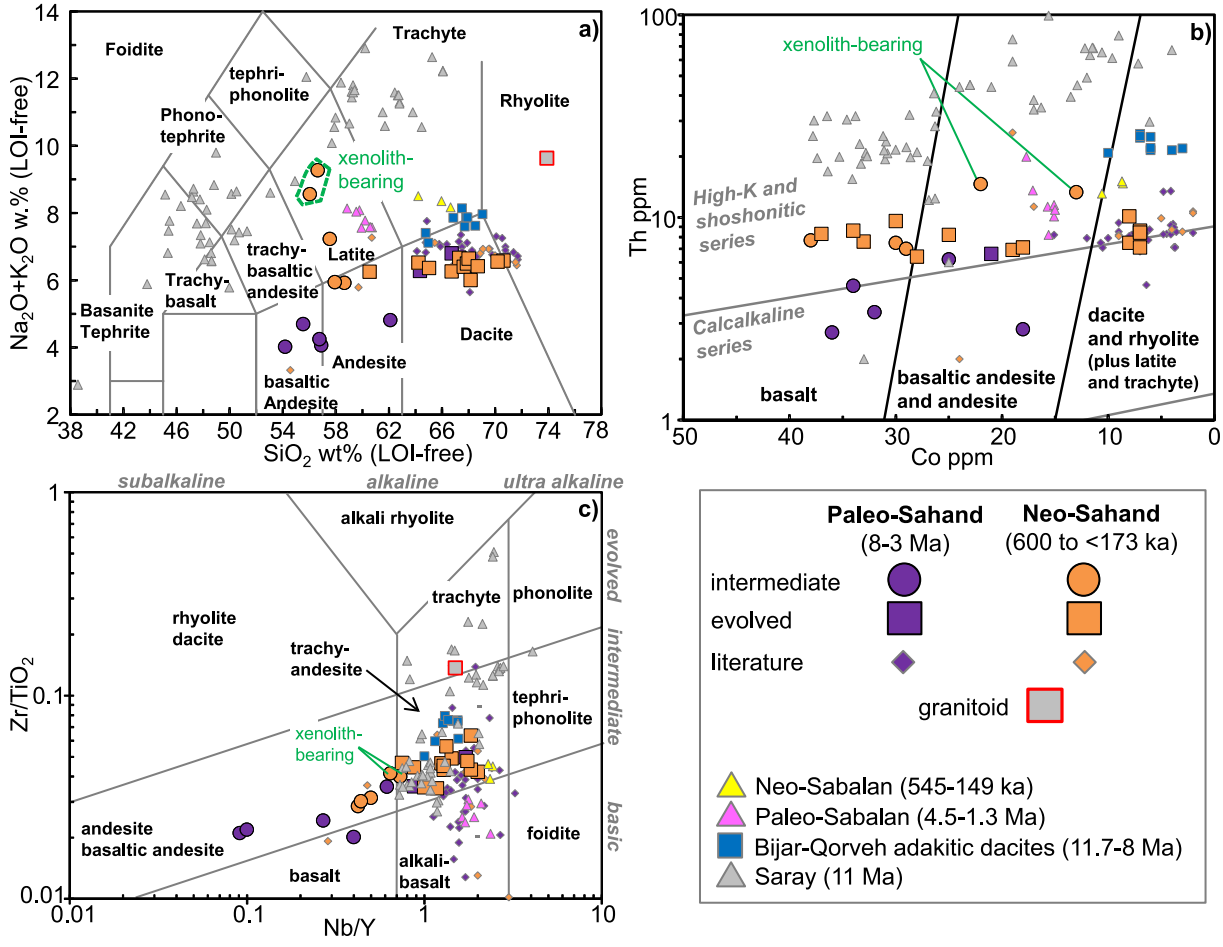


**Fig. 4.** a) Total Alkali vs Silica (Le Maitre, 2002), b) Th vs Co (Hastie et al., 2007) and c) $Zr/TiO_2$ vs Nb/Y (Pearce, 1996) classification diagrams for the investigated rock samples from the Sahand volcano. A highlight is provided for the two Neo-Sahand intermediate samples with quartzitic xenoliths. Also shown are literature data for the Paleo- and Neo-Sahand rock samples (Azizi and Moinevaziri, 2009; Ghalamghash et al., 2019; Lechmann et al., 2018; Pirmohammadi Alishah and Jahangiri, 2013), the products of the neighbouring Saray (Lustrino et al., 2019; Moayyed et al., 2008; Moghadam et al., 2014; Pang et al., 2013b) and Sabalan (with a distinction between the Paleo-Sabalan and Neo-Sabalan periods of activity; Dostal and Zerbi, 1978; Ghalamghash et al., 2016; Chaharlang et al., 2023) and the "adakitic" dacites from the Bijar-Qorveh area (Fedele et al., 2022). Low confidence literature data with LOI > 4.00 wt% and totals < 98 or > 102 were cautiously discarded.

Bijar-Qorveh area (Dehgholan and Qorveh locations, ~200 km to SE; Fedele et al., 2022), interpreted as the products of melting of an amphibolite source.

#### 4.3.1. Classification and serial affinity

The Sahand rocks span a wide compositional range (Fig. 4a). Paleo-Sahand intermediate rocks are poorer in $SiO_2$ (54.2–56.9 wt%, plus one sample with 62.1 wt%) and alkalis (4.02–4.69 wt%) with respect to Neo-Sahand intermediate rocks (respectively 56.1–58.7 and 5.92–9.27 wt%, with quartzitic xenoliths-bearing samples being the alkali-richest and silica-poorest; Fig. 4a). Evolved rock samples are more homogeneous and fall in the dacite field (64.4–70.6 wt% $SiO_2$, 6.00–6.80 wt% $Na_2O + K_2O$) with the exception of the silica-poorer (60.6 wt%) SM13–01 Neo-Sahand sample, classified as andesite. The granitoid sample shows a strongly evolved rhyolite composition with 73.9 wt% $SiO_2$ and 9.63 wt% $Na_2O + K_2O$. Literature data for the Sahand volcano mostly fall in the compositional group defined by the evolved samples, with only three Neo-Sahand rocks showing a less evolved basaltic andesite/andesite/latite composition.

Sabalan rocks are displaced towards higher alkali contents. The Bijar-Qorveh adakitic dacites cover a comparable silica range with respect to the evolved Sahand rocks, but have slightly higher sum of alkalis. The products of the Saray volcano are instead clearly different in terms of both degree of rock evolution (reaching near-primitive compositions) and silica saturation, defining an undersaturated to strongly undersaturated rock series.

Similar observations can be made using alternative classification plots based on "immobile" trace element ratios (Fig. 4b,c), proposed to remove the effects of post-depositional element mobilisation due to weathering and/or alteration processes. Indeed, Paleo-Sahand intermediate rocks are generally less evolved and appear to belong to an alkali-poorer magma series with respect to their Neo-Sahand counterparts. The xenolith-bearing Neo-Sahand samples appear enriched in elements/ratios indicative of alkali-richer affinity. A general increase in the alkalinity is again evident moving to Bijar-Qorveh, Sabalan (with Paleo-Sabalan products being less evolved than Neo-Sabalan ones) and Saray rocks.

#### 4.3.2. Major oxides and trace element contents

Harker variation plots for the investigated Sahand rocks generally depict poorly defined linear trends with increasing $SiO_2$. $TiO_2$, $Fe_2O_3$tot, MgO and CaO roughly decrease, while the behaviour of alkalis and $Al_2O_3$ is less clear (Fig. 5 and Fig. SM1 in Supplementary material 3). Intermediate rocks are always at the silica-poor and MgO-rich end and display some relatively large data scattering, particularly evident for $Al_2O_3$, CaO, $K_2O$ and $P_2O_5$. With the exception of the aforementioned silica-richest sample, Paleo-Sahand intermediate rocks are generally richer in $Al_2O_3$ (19.0–20.5 wt%) and CaO (7.46–8.58 wt%) and poorer in $SiO_2$, MgO (2.14–3.48 wt%) and $K_2O$ (0.96–1.30 wt%) with respect to Neo-Sahand ones (15.1–15.8 wt% $Al_2O_3$, 5.85–6.82 wt% CaO, 3.90–4.49 wt% MgO and 2.99–4.01 wt% $K_2O$). Compared to the latter, the xenolith-bearing Neo-Sahand intermediate samples are significantly richer in $Al_2O_3$, $K_2O$ and $P_2O_5$ and poorer in $Fe_2O_3$tot, MgO and CaO. The evolved rocks are more homogeneous and richer in $SiO_2$ and $Na_2O$, and poorer in $TiO_2$, $Fe_2O_3$tot and MgO, except the silica-poorest Neo-Sahand sample, commonly falling in between the two rock groups. Interestingly, evolved rocks define some evident linear arrays with very little scatter of data. The granitoid sample has the lowest $Al_2O_3$, $Fe_2O_3$tot, MgO and CaO and the highest $K_2O$. At comparable degrees of $SiO_2$ content, Sabalan rocks are slightly richer in $TiO_2$, $K_2O$, $Na_2O$ and $P_2O_5$, whereas Bijar-Qorveh adakitic dacites are enriched only in $K_2O$. Saray rocks are significantly K-richer and composed mostly of weakly evolved rocks, as previously remarked.

Plots of trace element abundances vs $SiO_2$ are significantly more scattered overall (Figs. 5 and SM2). Apart from being understandably richer in compatible elements such as Sc and V, Sahand intermediate rocks are richer in Y and poorer in Sr compared to the evolved rocks (20–26 vs 6–11 ppm and 331–453 vs 445–851 ppm, respectively). Compositional differences are much more subtle for numerous other elements such as Cr, Ni, Zr and Nb. These latter are generally slightly higher in Neo-Sahand than in Paleo-Sahand intermediate rocks, which are also poorer in Rb. The xenolith-bearing Neo-Sahand samples stand out mostly for their higher Rb (140–142 ppm), Sr (529–631 ppm), Zr (204–238 ppm) and Nb (18–19 ppm) and lower Sc (13–14 ppm) and V (146–162 ppm). Evolved rocks again define a much more homogeneous compositional group and again depict some regular trends with increasing rock differentiation. Remarkably, they have the typical "adakitic" signature, while the intermediate rocks fall in the field for "normal" arc rocks (ADR, andesite-dacite-rhyolite suite; Fig. 6a,b). The granitoid sample is rich in Rb, Zr, and Nb, and displays Y concentrations that are in between those of the intermediate and those of the evolved Sahand rocks. Sabalan rocks are richer in Sr and have slightly higher Nb at similar $SiO_2$ contents, while the adakitic rocks from Bijar-Qorveh are notably richer in Rb, Ba, Y and Zr than Sahand evolved rocks. Saray rocks have the highest concentrations in most trace elements (e.g., Sr, Ba, Zr, Y, Nb).

#### 4.3.3. Primitive mantle-normalised multielemental diagrams

As a whole, all Sahand samples display similar primitive mantle (PM) normalised patterns, mostly resembling the average estimate for the global subducting sediments (GloSS; Fig. 7a,b). These are characterised by high LILE (Large Ion Lithophile Elements) and low HFSE (High Field Strength Elements) abundances, with Pb peaks and Nb, Ta, P and Ti troughs. The most striking differences between intermediate and evolved rock samples are in the M-HREE (Middle-Heavy Rare Earth Elements) region. The first have higher abundances of both and nearly flat patterns, with $Dy_N/Yb_N$ of 0.99–1.18 (N for chondrite-normalised, using values from King et al., 2020), whereas are HREE-depleted ($Dy_N/Yb_N$ 1.28–1.71). The evolved rocks are also more enriched in Light REE (LREE), with $La_N/Yb_N$ 24.9–34.9 and $La_N/Sm_N$ 5.62–8.61 (vs 4.30–6.82 and 4.45–6.70 for the intermediate rocks). Further, the evolved rocks have small peaks at Eu [$Eu/Eu^* = Eu_N/(Gd_N{*}Sm_N)^{1/2}$] 1.00–1.10, except two samples with 0.96; while intermediate rocks have mostly Eu troughs (0.73–0.94, except two samples with 1.04).

Intermediate rocks from the Paleo-Sahand period are generally less enriched and display more pronounced Nb—Ta troughs and smaller Eu troughs (Eu/Eu* 0.73–0.77 vs 0.81–1.04) with respect to those from the Neo-Sahand. The two xenolith-bearing Neo-Sahand intermediate samples are the most enriched of all and display a small P peak. Again, an overall homogeneity is instead observed among evolved rocks. The granitoid sample has the strongest enrichment in the most incompatible elements, coupled with a peak at Zr—Hf, troughs at Ba and Eu (Eu/Eu* 0.39), and a concave-upward M-HREE pattern ($Dy_N/Yb_N$ 0.73).

Samples from the Sabalan (regardless of the period of activity) and the Bijar-Qorveh area are in line with evolved Sahand rocks (though slightly more enriched in all the "incompatible elements"), except for some small Eu trough in the Bijar-Qorveh adakitic dacites (Eu/Eu* 0.84–0.93; Fig. 7c). Saray rocks of comparable $SiO_2$ contents (~53–66 wt%) have much higher PM-normalised abundances and LREE/MREE ($La_N/Sm_N$ ~3–4) and LREE/HREE ($La_N/Yb_N$ ~20) enrichments that are halfway between those observed for the intermediate and evolved Sahand samples.

#### 4.3.4. Sr-Nd-Pb isotope systematics

The investigated Sahand rocks display variable $^{87}Sr/^{86}Sr_i$ ratios, mostly higher than the present-day estimate of BSE (Bulk Silicate Earth), coupled with more variable $^{143}Nd/^{144}Nd_i$ ratios, generally above the present-day estimate of ChUR (Chondritic Uniform Reservoir; Fig. 8a). Intermediate samples are more Sr-radiogenic ($^{87}Sr/^{86}Sr_i$ 0.70494–0.70585) than the evolved rocks (0.70437–0.70491), but the two groups show large overlap for $^{143}Nd/^{144}Nd_i$ (0.51259–0.51283 and

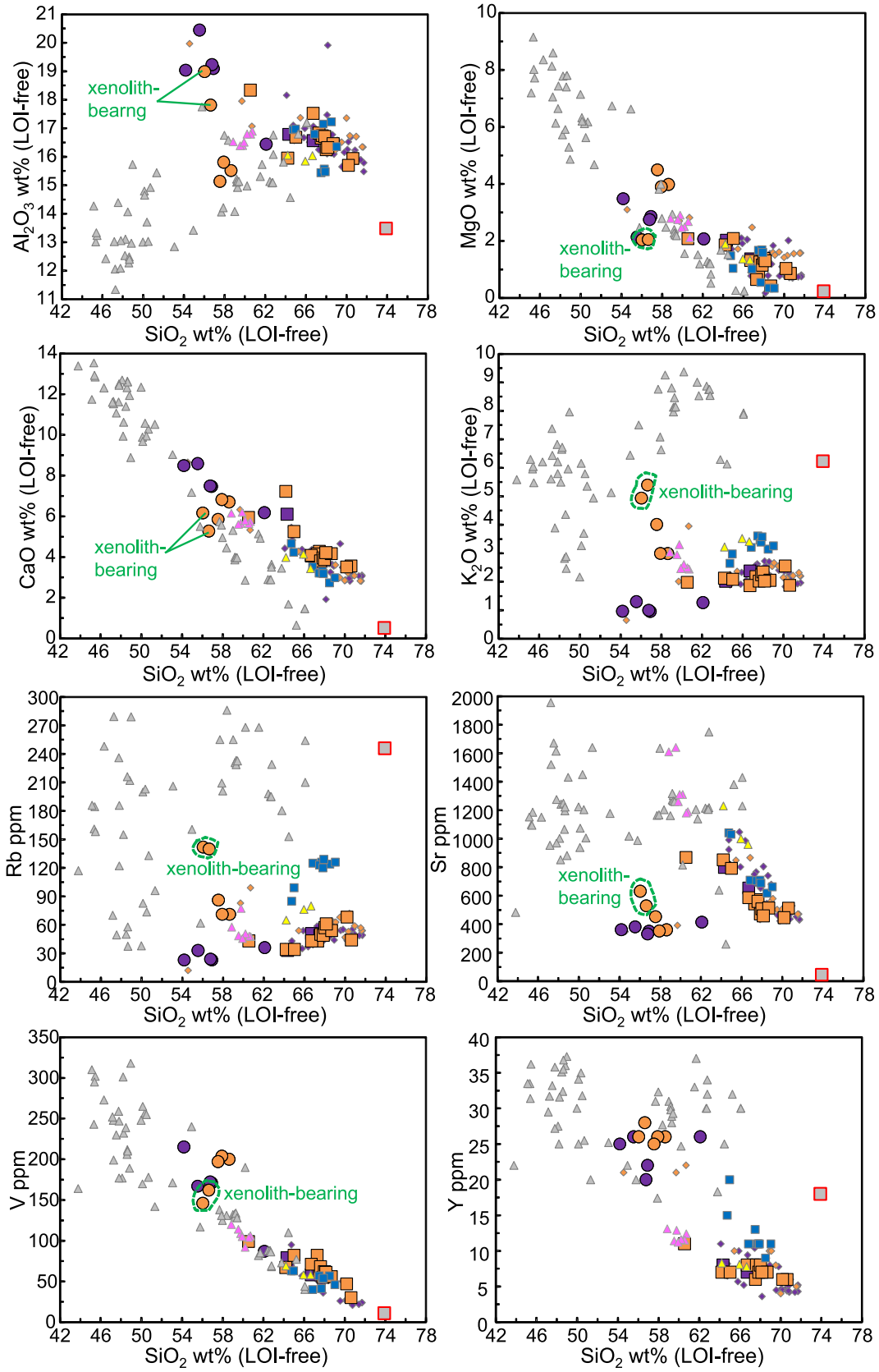


**Fig. 5.** Selected major oxides and trace elements vs $SiO_2$ diagrams for the investigated rock samples from the Sahand volcano. Symbols and source of literature data as in Fig. 4. Plots for the remaining oxides and trace elements are reported in Supplementary material 3 Fig. SM1 and SM2.

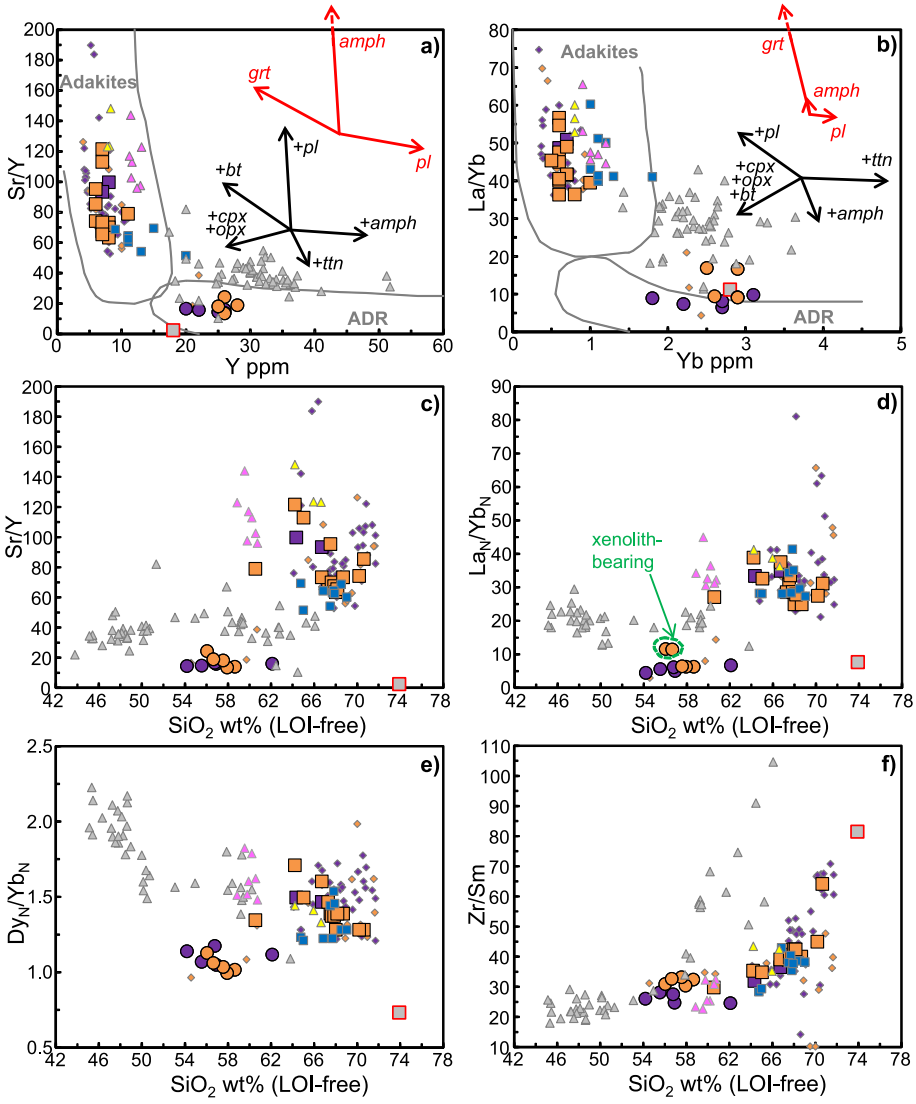


**Fig. 6.** a) Sr/Y vs Y, b) La/Yb vs Yb and c) Sr/Y, d) $La_N/Yb_N$, e) $Dy_N/Yb_N$ (N for chondrite-normalised, after King et al., 2020) and f) Zr/Sm vs $SiO_2$ diagrams for the investigated rock samples from the Sahand volcano. Symbols and source of literature data as in Fig. 4. In a) and b), the fields for adakites and "normal" arc andesite-dacite-rhyolite suites (ADR) are from Richards and Kerrich (2007) and the vectors showing the effects of the fractionation (red) or cumulation (black, marked with "+") of plagioclase (pl), amphibole (amph), garnet (grt), clinopyroxene (cpx), orthopyroxene (opx), biotite (bt) and titanite (ttn) are from Fedele et al. (2022). (For interpretation of the references to colour in this figure legend, the reader is referred to the web version of this article.)

0.51266–0.51295, respectively). In both cases there is no systematic difference between Paleo- and Neo-Sahand rocks. The $^{87}Sr/^{86}Sr$ and $^{143}Nd/^{144}Nd$ ratios measured for the granitoid sample are both extremely high, i.e. 0.714250 and 0.512964, respectively. If corrected assuming an Eocene age (45 Ma), the first decreases significantly ($^{87}Sr/^{86}Sr_{45Ma}$ = 0.70413), while $^{143}Nd/^{144}Nd_{45Ma}$ remains roughly unchanged (0.51293; Fig. 8a). On the other hand, when corrected for the ages of the beginning of the Paleo-Sahand (8 Ma) and Neo-Sahand periods (0.6 Ma), the granitoid sample displays high $^{87}Sr/^{86}Sr_i$ (0.71245 and 0.71412) at similar $^{143}Nd/^{144}Nd_i$ ~0.51296. Overall, isotope ratios for Sahand rocks are consistent with those of literature UDMA rocks. Paleo-Sabalan and Neo-Sabalan Sr—Nd isotope data are indistinguishable from each other ($^{87}Sr/^{86}Sr_i$ 0.70444–0.70451, $^{143}Nd/^{144}Nd_i$ ~0.51276) and overall in line with Shand evolved rocks. Both Saray rocks and Bijar-Qorveh adakitic dacites are remarkably more Sr-radiogenic and Nd-unradiogenic (0.70662–0.70807 vs 0.51240–0.51252 and 0.70738–0.70773 vs 0.51238–0.51242, respectively).

Lead isotope ratios are rather homogeneous for $^{206}Pb/^{204}Pb_i$ (18.81–18.90), with more variable $^{207}Pb/^{204}Pb_i$ (15.61–15.72) and $^{208}Pb/^{204}Pb_i$ (38.84–39.19), falling between the GloSS and DMM (Depleted MORB Mantle) end-members (Fig. 8b,c). Albeit with some overlap, Paleo-Sahand samples tend to be more enriched in uranogenic and thorogenic lead compared to Neo-Sahand ones. The Pb isotope values for the granitoid sample are in line with those of the latter, and do not change significantly as a function of the recalculated age. All the samples plot above the Northern Hemisphere Reference Line (NHRL) and show positive Δ7/4 (8.5–17.3, 7.4 for the granitoid at 45 Ma) and Δ8/4 (49.5–60.6 and 48.3). Compositions are consistent with those of the literature UDMA rocks. Saray have slightly (though clearly) more radiogenic $^{206}Pb/^{204}Pb_i$ (19.10–19.26) and $^{208}Pb/^{204}Pb_i$ (39.27–39.46), pointing towards the HiMu (High μ, i.e. $^{238}U/^{204}Pb$) end-member.

## 5. Discussion

### 5.1. The relationships between the intermediate and the evolved Sahand rocks

At a first glance, the overall petrographic and mineral chemical features of Sahand intermediate and evolved rocks are consistent with some genetic linkage, obviously supported also by their spatial and temporal association. The intermediate rock samples are indeed characterised by mineral assemblages richer in anhydrous ferromagnesian minerals, whereas the evolved rocks are dominated by more sodic plagioclase and include mostly hydrous ferromagnesian minerals. Whole-rock geochemistry is also roughly in line with this, as the intermediate rock samples are clearly richer in "compatible" $TiO_2$, $Fe_2O_3$tot, MgO, CaO, Sc and V.

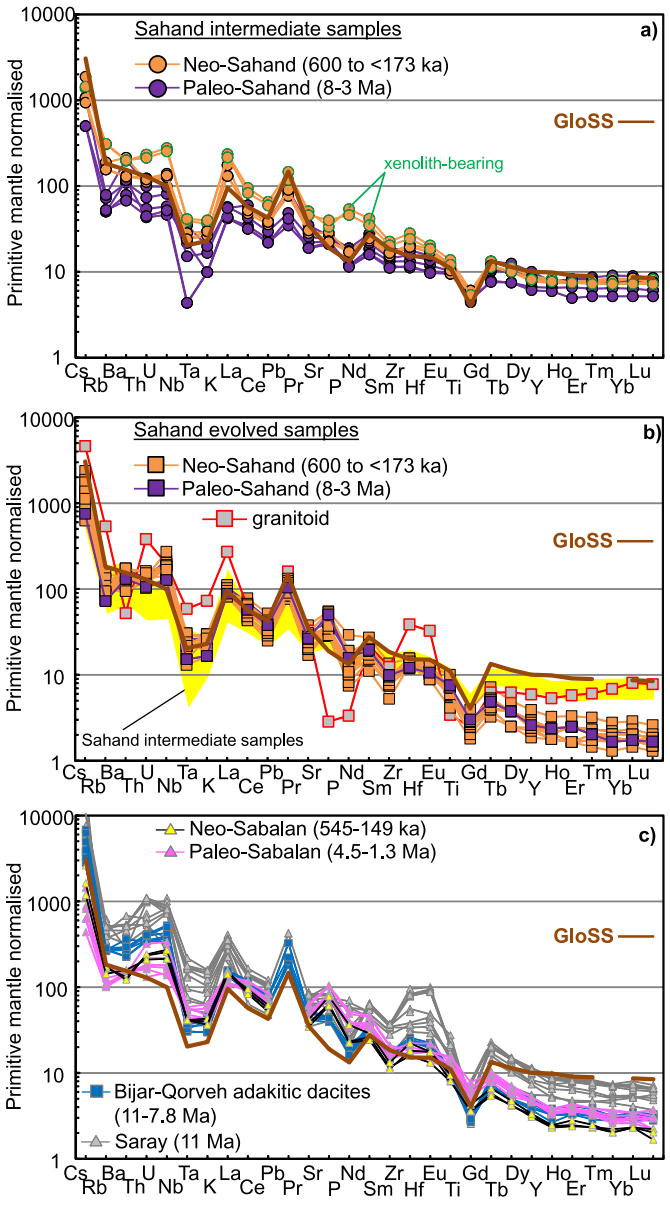


**Fig. 7.** Primitive mantle-normalised (after Lyubetskaya and Korenaga, 2007) multielemental plots for the investigated a) intermediate (with a highlight on two xenolith-bearing samples) and b) evolved (including the granitoid) rock samples from the Sahand volcano and for c) literature data for the Sabalan and Saray rocks (~53–66 wt% $SiO_2$) and for the Bijar-Qorveh adakitic dacites (sources as in Fig. 4). Average Global Subducting Sediments composition (GloSS) is from Plank (2014).

Nevertheless, the abrupt increase in Sr from intermediate (mostly < 440 ppm, excluding the two xenolith-bearing samples) to evolved compositions (870 ppm) at ~60 wt% $SiO_2$ cannot be explained with fractionation processes of the plagioclase-dominated parageneses observed in the investigated samples, considering $D_{Sr}^{pl/melt}$ being around 2 for basaltic andesite systems (e.g., Laubier et al., 2014). The constant Eu/Eu* close to unity of the evolved rocks also argues against plagioclase fractionation. Further, moving from the intermediate to the evolved rocks, Y shows an abrupt decrease, again at ~60 wt% $SiO_2$. This would require abundant amphibole fractionation, given that $D_Y^{amph/melt}$ increase from 2.5 to 9.7 from andesitic to rhyolitic liquids (Nandedkar et al., 2016). On the other hand, plagioclase fractionation would produce the opposite effect, increasing Y concentrations in residual melts due to its strong incompatibility in this phase (e.g., Laubier et al., 2014).

It seems therefore reasonable that the intermediate and evolved rocks from the Sahand volcano are not genetically linked, differently from what previously proposed by Ghalamghash et al. (2019). This is also suggested by Sr isotopes, as evolved compositions have lower $^{87}Sr/^{86}Sr_i$ compared to intermediate rocks, which is inconsistent with typical differentiation processes, either operating in closed-system (which would preserve the $^{87}Sr/^{86}Sr_i$ of the parent magma) or in open-system conditions (typically increasing the $^{87}Sr/^{86}Sr_i$ of the contaminated, Si-richer magmas).

On such basis, the high Sr/Y (> 60) and La/Yb (> 35) of the evolved rocks, coupled with low Y and Yb (Fig. 6a,b), could not be acquired by a "normal" calcalkaline magma through fractionation at lower crustal depths, as proposed in other cases where "adakitic" and "non adakitic" rocks are in close temporal and spatial association (e.g., Rodríguez et al., 2007). The presence of both adakitic and non-adakitic magmas emplaced throughout the entire history of the Sahand volcano instead requires the presence of two independent magma batches. This would also explain the lack of any spatial (e.g., related with specific structural features) and/or temporal control in the transition from adakitic to non-adakitic magmatism (or vice versa), generally observed where adakitic and non-adakitic magmas are derived from the same parental magmas differentiating at high (through garnet- and/or amphibole-dominated fractionation) and low crustal levels (plagioclase-dominated fractionation; e.g., Macpherson et al., 2006; Chiaradia et al., 2009; Kolb et al., 2013; Marchev et al., 2013).

### 5.2. Petrogenesis of Sahand evolved rocks

As derivation from the intermediate rocks through magma differentiation processes can be safely ruled out for the evolved rocks, a question arises as for their origin. The compositions of the Paleo- and Neo-Sahand evolved rocks are largely overlapping, suggesting that conditions that led to their generation did not substantially change with time. Their adakitic geochemical fingerprint likely points to partial melting of a (meta-) basalt/pelite/greywacke source leaving amphibole and/or garnet in the solid residue (see, e.g., Moyen, 2009). The high silica content of Sahand evolved rocks clearly excludes an origin from a mantle region that interacted with adakitic melts [as instead proposed for the LSA - low-silica adakites sensu Moyen, 2009], and therefore indicates derivation from a crustal source. An origin from melting of a metabasalt source is the most likely possibility, as proposed for the "true" adakites (or HSA - high-silica adakites *sensu* Moyen, 2009). Indeed, Sahand evolved rocks satisfy many of the geochemical requirements for such kind of rocks (e.g., Castillo, 2012; Moyen, 2009), including: 1) $SiO_2$ > 56 wt%, $Al_2O_3$ > 15 wt%, MgO < 3 wt% and $Na_2O$ > 3.5 wt%; 2) Sr > 400 ppm, Y < 18 ppm, Yb < 1.8 ppm; 3) Sr/Y > 20 and La/Yb > 20.

The igneous activity of Sahand was entirely successive to the inception of the Iran-Arabia collisional stage (see Section 2). Therefore, it seems unlikely that Sahand adakitic melts were sourced from the contemporaneous subduction of the Neotethyan slab, which would also be inconsistent due to their relatively high Sr and low Nd isotopic compositions. A more reasonable source could be the lower crust, provided that melting depths were sufficient for melts to equilibrate with a residuum with < 20 wt% of plagioclase (i.e., mostly between 30 and 40 km, at ~1.0–1.2 GPa; Qian and Hermann, 2013). Such conditions seem compatible with local geology, as crustal thickness of ~45 km is reported for the Sahand-NW Iran area (e.g., Priestley et al., 2012; Stern et al., 2021, and references therein).

### 5.3. Geothermobarometric estimates

Several geothermobarometric algorithms were applied to the investigated Sahand rocks, fully presented in the Supplementary material 1. Although a careful preliminary check was undertaken to filter out mineral data referring to crystals in textural and/or chemical

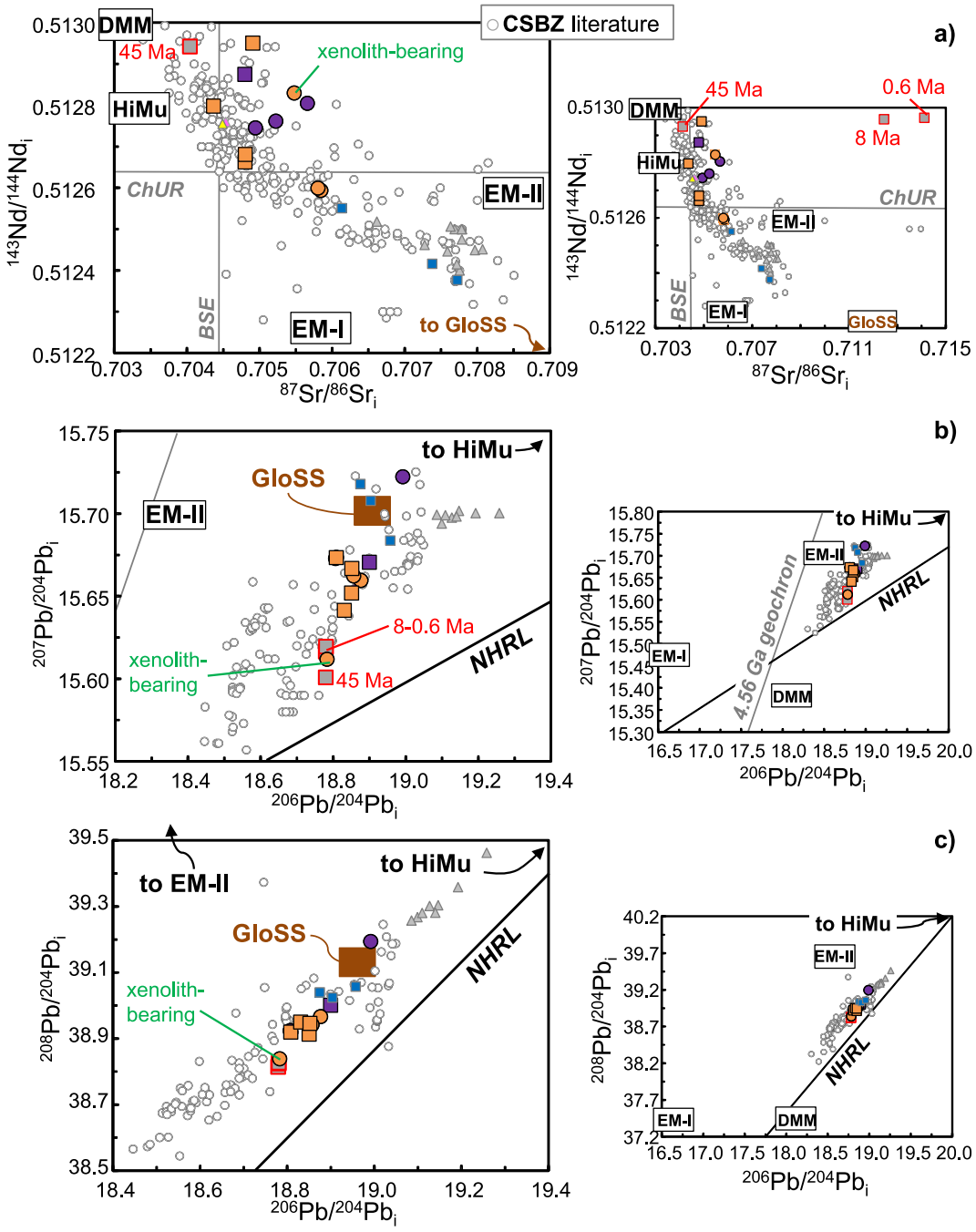


**Fig. 8.** a) $^{143}Nd/^{144}Nd_i$ vs $^{87}Sr/^{86}Sr_i$, b) $^{207}Pb/^{206}Pb_i$ vs $^{206}Pb/^{204}Pb_i$ and c) $^{208}Pb/^{206}Pb_i$ vs $^{206}Pb/^{204}Pb_i$ diagrams for the investigated rock samples from the Sahand volcano, both with a larger view and a close-up. Symbols and literature data as in Fig. 4. The three data for the granitoid sample (overlapping in c) refer to three different age corrections (0.6, 8 and 45 Ma). Literature data for the Cenozoic subduction-related Bitlis-Zagros suture igneous rocks (CSBZ, white circles) are from the database of Lustrino et al. (2021). Chondritic Uniform Reservoir (ChUR), Bulk Silicate Earth (BSE), Northern Hemisphere Reference Line (NHRL), Depleted MORB Mantle (DMM), Enriched Mantle types I and II (EM-I and EM-II) and High μ (high $^{238}U/^{204}Pb$; HiMu) are from Lustrino and Anderson (2015). Average Global Subducting Sediments composition (GloSS) is from Plank (2014).

disequilibrium, the results are not always unequivocal. A main reason for this could be related to the use of whole-rock data as a proxy for melt composition, which appears highly dubious due to the relatively high phenocryst load. The two xenolith-bearing samples are even less appropriate, as their whole-rock composition has been demonstrated to be evidently modified by xenolith partial digestion. In addition, different mineral phases have different (and possibly wide) ranges of crystallisation, and therefore might provide only a limited picture of the crystallisation conditions, if the amount of collected data is not sufficiently large to ensure statistical representativity.

In order to circumvent these issues, a choice was made to focus on data obtained from amphibole chemistry, using the "amph-only" geothermobarometer of Ridolfi et al. (2010). Indeed, amphibole is generally the first phase that crystallises in adakitic magmas, as well as in water-saturated intermediate to evolved magmas in general, at a wide range of crustal depths (e.g., Alonso-Perez et al., 2009; First et al., 2021; Prouteau and Scaillet, 2003). For this reason, amphibole compositions have been successfully used to obtain information on the composition and intensive parameters that characterised "adakitic" melts (e.g., Ribeiro et al., 2016; Tang et al., 2017; Wang et al., 2021).

The results of geothermobarometric calculations for Sahand rocks define some very regular trends of decreasing P and T conditions (Fig. 9), indicating a large range of amphibole crystallisation, between 760 and 96 MPa (i.e., ~29 to ~3.6 km of depth) and 1003 to 794 °C. Intermediate rocks seem to have crystallised in a more restricted depth range, between ~22 and ~11 km (at 571–289 MPa and 993–928 °C). The decrease in depth values observed from Neo-Sahand to Paleo-Sahand samples is clearly related with the paired decrease of MgO, pointing to an increase in the degree of evolution of the host rock. The same trend can be observed for the evolved rocks, in which amphibole appears to have crystallised in a much larger depth interval. The silica-poorest Paleo-Sahand sample includes amphiboles crystallised at ~17–9 km, plus two crystal cores that indicate deeper equilibration (~29–28 km). The evolved Neo-Sahand samples with similar $SiO_2$ contents have amphibole crystals that seem to have equilibrated at comparable depths (~16–11 km), while the silica-richest include mostly crystals that equilibrated at very shallow depths (~7–4 km). These observations thus point to a model of polybaric magma differentiation linking Sahand evolved rocks. This is evident for the Neo-Sahand rocks only, as amphibole data for the Paleo-Sahand rocks refer to one single sample. Nevertheless, based on the numerous similarities for the evolved rocks of the two periods, we feel safe to consider that the two rock groups experienced similar petrogenetic processes.

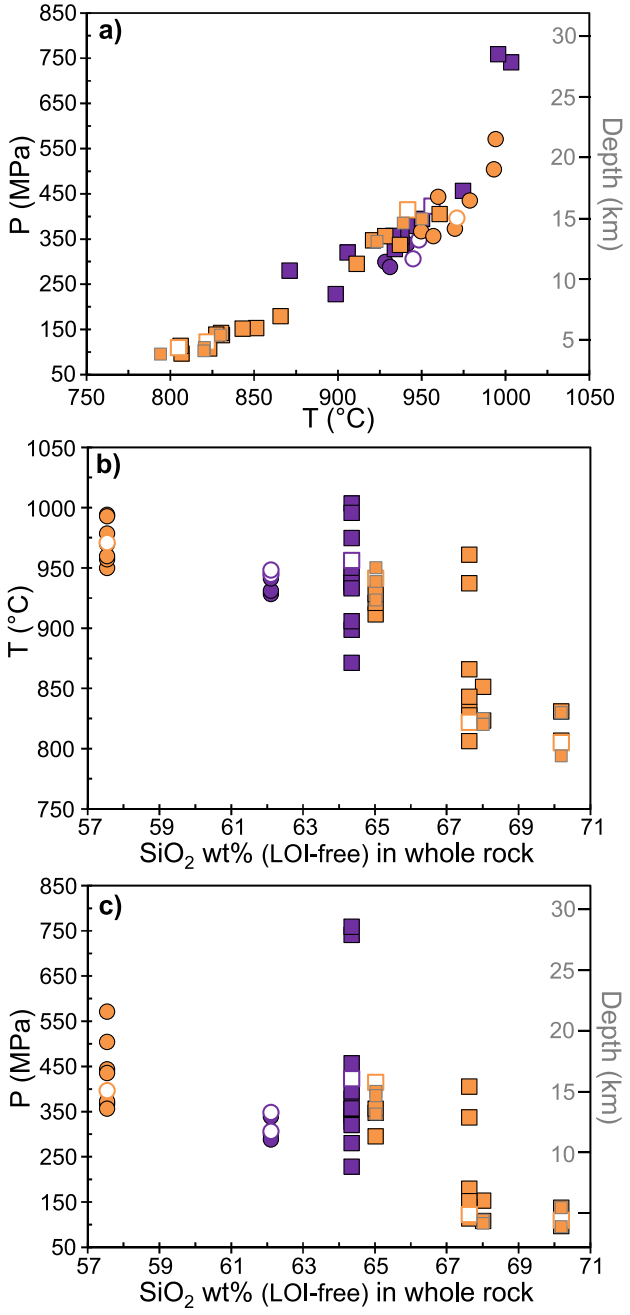


**Fig. 9.** a) Pressure/depth vs temperature and b) temperature and c) pressure/depth vs $SiO_2$ in whole-rock for the amphibole crystals from the investigated rock samples from the Sahand volcano. Symbols as in Fig. 3. Estimates of P and T were obtained using the equations from Ridolfi et al. (2010), as reported in the Supplementary material 1.

In such a framework, the two amphibole cores from the Paleo-Sahand evolved sample yielding the highest equilibration P and T could represent the very first stages of evolution, when adakitic magmas had just separated from their lower crustal source, at depths of ~30 km. During their ascent, magmas differentiated at variable middle to upper crustal conditions, likely in closed-system conditions mainly, according to the numerous nicely correlated binary variation diagrams. However, crustal interaction cannot be completely ruled out, as it could be obscured when the contaminant is not substantially different from assimilating magma. This might be the case for the Sahand, where the basement is known to include Eocene volcanic products (see Section 2.2).

### 5.4. *The differentiation of Sahand evolved magmas*

Major oxide and trace element trends for Sahand evolved rocks are mostly coherent and largely rather continuous, with the only exception of the silica-poorest andesitic Neo-Sahand sample (SM13–01, 60.6 wt% $SiO_2$), which is clearly separated from all the other samples (in the ~64–70 wt% $SiO_2$ range). It is therefore at least dubious whether this sample belongs to the same magmatic lineage. We thus cautiously exclude it from our observations and propose some tentative explanations only in a later section of this paragraph.

Differentiation trends are strongly suggestive of a plagioclase- and amphibole-dominated fractionation, as indicated by decreasing $Al_2O_3$, $Fe_2O_3$tot, MgO, CaO, Sr, Ba, Sc, V and Y (the latter very faintly; Figs. 5 and SM2), and in accordance with petrographic evidence. The relative role of these phases can be qualitatively assessed considering key trace element ratios (Fig. 6). The main control seems to be played by plagioclase, given the linear decrease of the Sr/Y and $La_N/Yb_N$, as both would instead increase (especially the first) in an amphibole-dominated fractionation process (e.g., Fedele et al., 2022; Fig. 6a,b,c,d). On the other hand, the decrease of $Dy_N/Yb_N$ and the increase of Zr/Sm (Fig. 6e, f) testify for significant amphibole fractionation, given its high partition coefficients for MREE (e.g., Nandedkar et al., 2016) compared to plagioclase (Aigner-Torres et al., 2007; Laubier et al., 2014).

An attempt to a quantitative assessment of differentiation processes was also undertaken, first assuming a simple closed-system mass-balance model. The results indicate that the transition from the silica-poorest dacite to the silica-richest dacite/rhyolite evolved Sahand samples can be very satisfactorily reproduced ($\Sigma R^2 < 0.4$) by ~23 wt% fractionation of an assemblage consisting of plagioclase (~44 wt%), amphibole (~36 wt%), biotite (~15 wt%) and accessory Ti-magnetite and apatite (Supplementary material 1).

Nevertheless, isotope geochemistry suggests that concurrent open-system processes were likely active. Magma differentiation was indeed accompanied by an overall increase of $^{143}Nd/^{144}Nd$ and a clear decrease of $^{207}Pb/^{204}Pb$ values (Figs. 10 and SM3). The granitoid sample could be a reasonable proxy for a contaminant, based on the values of its isotope ratios corrected at the age of the Paleo- and Neo-Sahand periods, and on its major oxides and trace element geochemistry. This sample indeed commonly falls at the silica-richest end of the liquid line of descent defined by Sahand evolved samples, except for its higher Y, HFSE and Th (Figs. 5, SM1 and SM2). The 8 and 0.6 Ma age-corrected $^{87}Sr/^{86}Sr$ for this granitoid are also extremely high (see Section 4.3.4 and Fig. 8), but

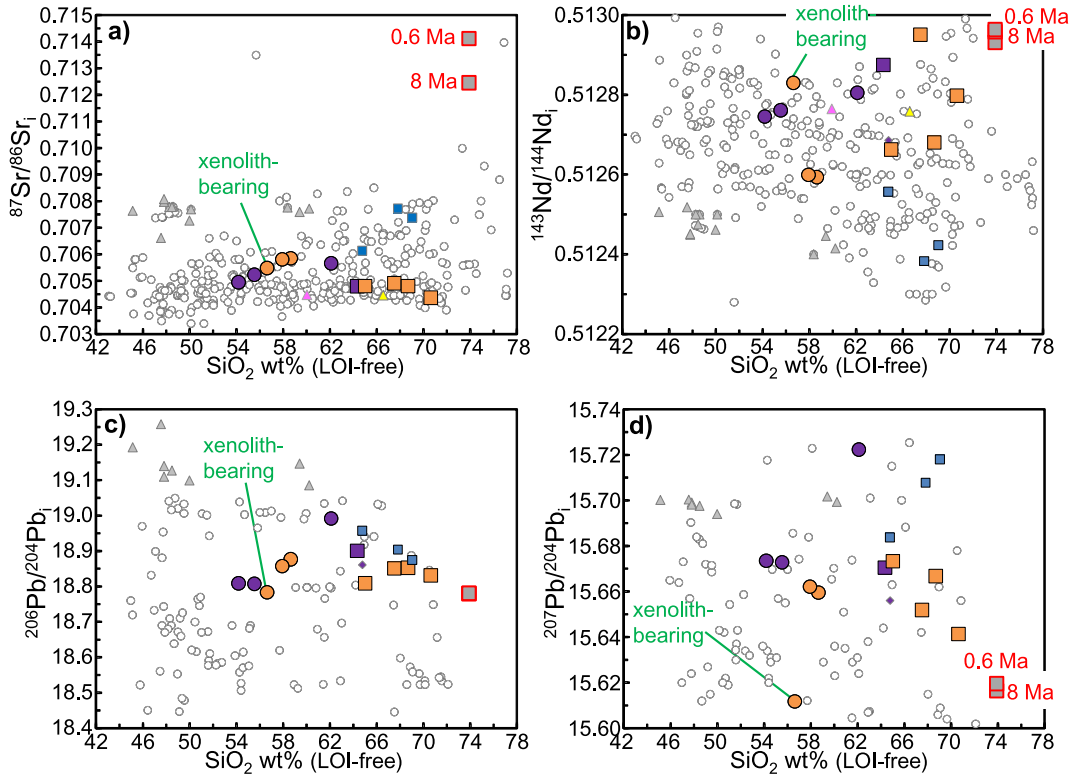


**Fig. 10.** a) $^{87}Sr/^{86}Sr_i$, b) $^{143}Nd/^{144}Nd_i$, c) $^{206}Pb/^{204}Pb_i$ and d) $^{207}Pb/^{204}Pb_i$ vs $SiO_2$ for the investigated rock samples from the Sahand volcano. Symbols and literature data as in Fig. 8. The two data for the granitoid sample (overlapping in c) refer to age corrections at 0.6 and 8 Ma. The diagram for $^{208}Pb/^{204}Pb_i$ is reported in Supplementary material 3 Fig. SM3.

were likely insufficient to affect evidently the values of the contaminated magmas, given the significantly lower Sr (45 ppm vs 445–851 ppm in Sahand evolved rocks). On the other hand, the elemental Nd is comparable (22 vs 11–22 ppm) and Pb is slightly higher (23 vs 11–19 ppm), thus justifying the stronger effect on the isotope ratios for these elements. Models of combined assimilation and fractional crystallisation are only qualitatively in line with this, but also indicate that the petrogenesis of Sahand evolved rocks was likely more complex, possibly involving isotopically inhomogeneous sources and/or contaminants (Figs. SM4 and SM5).

In this framework, the andesitic evolved sample could indicate an earlier stage in magma differentiation. During this stage, the strong increase of Sr/Y, $La_N/Yb_N$ and $Dy_N/Yb_N$ and the small increase of Zr/Sm would suggest garnet fractionation leading to the composition of Sahand dacitic evolved rocks (Fig. 6). Indeed, Y and HREE are strongly partitioned in garnet, while Zr and Sm have a similar incompatible behaviour (e.g., Pertermann et al., 2004). Quantitative modelling for the transition from this andesitic sample to the silica-poorest dacite sample indicates that ~25 wt% fractionation of an assemblage made of plagioclase (~70 wt%), amphibole (~8 wt%), garnet (~13 wt%), Ti-magnetite (~9 wt%) and accessory apatite could explain major oxides concentrations of the evolved samples. The andesitic sample would thus represent the "original" adakitic melt generated by partial melting of the lower crust, which would have first stalled at lower crustal depths and fractionated a garnet-bearing assemblage, eventually reaching sufficient buoyancy to upwell towards shallower levels. The lack of any petrographic evidence for garnet fractionation is not surprising because the presence of garnet in adakitic rocks is reported very rarely (e.g., Wang et al., 2021). Indeed, garnet fractionation has been mostly inferred indirectly based on whole-rock geochemical evidence only, the process being largely "cryptic" due to the high density of the mineral preventing its permanence in the upwelling melts. Nevertheless, reports of garnetite cumulate layers in exposed lower crustal sequences (e.g., Khoistan island arc, Pakistan, North Qaidam ultra-high pressure metamorphic belt, NW China; Jagoutz et al., 2009; Song et al., 2014) provided empirical indirect supporting evidence.

An alternative and intriguing possibility is that the andesitic evolved sample is rather the product of the mixing between "adakitic" and "non-adakitic" melts, as its composition invariably lies in an intermediate position between the intermediate and evolved Sahand samples. The lack of any interaction between the two melts seems indeed unlikely, considering that both appear to have been generated throughout the entire eruptive history of the Sahand volcano, and that comparable crustal depths of equilibration are indicated by amphibole geothermobarometry.

### 5.5. *Petrogenesis of Sahand intermediate rocks*

Compared to the evolved "adakitic" rocks, the intermediate rocks are much less represented in the Sahand volcano (especially in the existing literature). To complicate the general framework, basic, near-primitive compositions are completely absent, making a detailed reconstruction of the petrogenetic processes responsible for the genesis of Sahand intermediate rocks not possible. Nevertheless, some general inferences can still be made based on the new datasets presented here.

Some systematic differences were observed between Paleo- and Neo-Sahand intermediate rocks, the first showing a relatively wider range of silica compositions and linear differentiation trends. Fractionation of plagioclase, clinopyroxene orthopyroxene and Ti-magnetite, joined in later stages by amphibole, was likely active (e.g., decreasing $TiO_2$, $Fe_2O_3$tot, MgO, CaO, Sc and V, increasing Rb, Sr, Ba and $La_N/Yb_N$, and constant Sr/Y, $Dy_N/Yb_N$ and Zr/Sm; Figs. 5, 6, SM1 and SM2), in line with petrographic observations. Based on the increase in Sr and especially Pb isotope ratios (at roughly constant $^{143}Nd/^{144}Nd_i$) with increasing degree of evolution (Figs. 10 and SM3), it seems likely that fractionation was accompanied by assimilation of an upper crustal

contaminant that was different from the one proposed for the evolved rocks.

The relatively large compositional variation of Neo-Sahand samples is ascribable to the presence of two xenolith-bearing samples, characterised by enrichment in alkalis, $Al_2O_3$, $P_2O_5$, Rb, Ba and Sr, and coupled depletion in $Fe_2O_3$tot, MgO, CaO, Sc and V. Only one of the two xenolith-bearing samples was analysed for isotopic ratios, and it shows the highest $^{143}Nd/^{144}Nd_i$ and the lowest $^{206}Pb/^{204}Pb_i$, $^{207}Pb/^{204}Pb_i$ and $^{208}Pb/^{204}Pb_i$. Despite Nd and Pb isotope ratios being in line with those of the Eocene granitoid, major oxide and trace element constraints (above all, the higher $Al_2O_3$, Ba and Sr compared with the remaining Neo-Sahand intermediate rocks) exclude any significant assimilation of the latter. These also suggest that the quartzitic xenoliths do not represent in full the nature of the assimilated crustal lithologies, part of which must have been digested by the intruding magma. Therefore, we can only speculate that the assimilant was likely represented by rocks cogenetic with the granitoid sample, but less evolved in composition. In any case, it is clear that the whole-rock compositions of the two xenolith-bearing samples were significantly modified by the entrainment of such xenoliths, and therefore will not be considered further.

The remaining Neo-Sahand intermediate samples are clearly different from their Paleo-Sahand counterparts, mainly for their lower $Al_2O_3$ and stronger enrichment in $K_2O$ and incompatible elements. These observations, corroborated by the presence of groundmass alkali feldspar, could be taken as evidence that Neo-Sahand intermediate rocks belong to a slightly alkali- and K-richer magma series. Both series are clearly related to parental melts that originated from a subduction-modified mantle source (Fig. 7). The increase in alkalinity and in incompatible elements contents with time could reflect activation of similar mantle source regions with increasing contributions from the K- and incompatible elements-bearing metasomes, or polybaric melting of a compositionally heterogeneous source, as proposed for some Cenozoic districts of the Italian Peninsula (e.g., Lustrino et al., 2011; Peccerillo, 2017). Although the lack of near-primitive compositions precludes the possibility to investigate this further, it is worth noting that similar time-related trends have not been reported so far for the nearby, roughly coeval Saray and Sabalan volcanoes, possibly suggesting that local geology played a major role. This will be evaluated in the following sections.

### 5.6. A comparison with coeval neighbouring magmatism: The Saray-Sahand-Sabalan alignment and the Bijar-Qorveh adakitic dacites

Lechmann et al. (2018) observed that the wide compositional variability that characterised the Miocene-Quaternary magmas emplaced in NW Iran is coupled with no clear temporal and/or geographical trends. They used this evidence to exclude simple models of magmatism associated with slab retreat or lithospheric delamination, preferring the presence of heterogeneously metasomatised mantle and crustal components to explain the magmatic diversity. Similarly, the absence of any direct correlation between magma productivity (in terms of ore mineralization) and adakitic magmas emplaced in NW Iran, led Rabiee et al. (2022) to also invoke variable petrogenetic processes for each sector of such a tectonically complex area. On the other hand, Ghalamghash et al. (2019) recognised a rough trend of time progression defined by the Saray-Sahand-Sabalan alignment, and interpreted this as reflecting the progressive roll-back of the subducted Neotethyan slab, followed by its break-off and subsequent asthenospheric upwelling, the latter acting as a trigger for melting processes.

To shed light on such controversies, we focus on the Saray-Sahand-Sabalan alignment (marking a broad array of increasing distances from the Neotethyan suture zone) and on the Bijar-Qorveh area, which is roughly at the same distance from the suture with respect to Sahand and includes both adakitic and non-adakitic calcalkaline rocks. The chosen areas are among the neighbouring magmatic districts that have been studied in more detail.

#### 5.6.1. Regional trends in magma compositions

While the products of the Sahand and Sabalan volcanoes share numerous petrographic and geochemical similarities (see Section 4), magmatism at the Saray was clearly different and remarkably K-richer, featuring: 1) trachytic dikes, 2) leucite-bearing basanitic-tephritic-trachytic-phonolitic rocks, 3) leucititic lavas and 4) sannaitic lamprophyres (Lustrino et al., 2019; Moghadam et al., 2014; Pang et al., 2013b). This suggests derivation from mantle source regions that were more intensely modified by subduction-related metasomatic agents (in line with their extreme enrichment in incompatible elements and their marked Sr- and Pb-radiogenic and Nd-unradiogenic composition) with respect to Sahand and Sabalan rocks. An explanation for such exclusive peculiarity could lie in the more proximal position of the Saray volcano with respect to the suture zone. Indeed, the thickness of the mantle wedge is expected to increase from the SW to the NE, and thus the relative volume of the metasomes would decline in the same direction, from Saray to Sabalan (Fig. 11). As a result, when conditions for mantle melting were attained, the contribution from the K- and incompatible elements-richer metasomes (veins) to the newly produced melts would be progressively more diluted with increasing distance from the suture.

Although the above model is consistent with the change in rock composition observed moving from Saray to Sahand, no such trend is evident moving from Sahand to Sabalan. The increasing thickness of the local crust, from ~38 km (beneath Saray), to ~45 km (Sahand) and up to ~53 km (Sabalan; Ghalamghash et al., 2019 and references therein) may have played a major role. The high-K Saray magmas should have crossed average thickness crustal sections quite easily, as also testified by the common presence near-primitive rock compositions. These latter are not observed at Sahand and Sabalan, testifying for a stronger density filtering due to the thicker local crust. Worth of note, the decrease in $K_2O$ with increasing distance from the suture is the opposite of what was historically expected in magmatic arcs, further supporting the idea that in collisional contexts crustal thickness has a stronger influence on other geochemical parameters (mainly Sr/Y and La/Yb; see Luffi and Ducea, 2022 for a review).

In the Sahand case, rocks representing either differentiated melts from mantle-derived magmas (i.e., the intermediate rocks) or melts from the lower crust (the evolved “adakitic” rocks) are present. The latter could have formed as consequence of the heat released by the former during their upwelling to shallower levels (Fig. 12). Both melt types then stalled at variable crustal depths and differentiated via AFC, possibly interacting to produce hybrid melts (i.e., the andesitic Neo-Sahand evolved sample). On the other hand, non-adakitic compositions have never been reported so far at the Sabalan. The genesis of Sabalan magmas was first ascribed by Ghalamghash et al. (2016) to high degrees partial melting of a metasomatised mantle source, followed by closed-system evolution. Very recently, Chaharlang et al. (2023) rather invoked partial melting of a garnet amphibolite thickened lower crustal source (followed by fractional crystallisation of clinopyroxene, plagioclase and amphibole), like what has been proposed here for Sahand evolved rocks. However, the lack of detailed mineral chemistry and Sr-Nd-Pb isotope data for Sabalan rocks does not allow further comparisons with the Sahand case, despite the numerous whole-rock similarities of the two adakitic rock types. We can speculate that the absence of non-adakitic melts at the Sabalan could be evidence for a very efficient density filtering due to the higher crustal thickness. There, mantle-derived melts would have provided heat for lower crustal melting (as for the Sahand), and then would have stalled and differentiated at depth, eventually solidifying completely before reaching the surface.

Although the crucial role of crustal thickness emerges clearly, it seems likely that crustal composition also influenced the composition of the volcanic rocks in NW Iran, as the two volcanoes lie on different sides of the Tabriz fault [Fig. 1a; see also Rabiee et al., 2022]. This is further indicated by the Miocene subduction-related magmatism in the Bijar-Qorveh area. The adakitic rocks of this district have shown numerous geochemical differences compared to the Sahand adakitic rocks (mainly

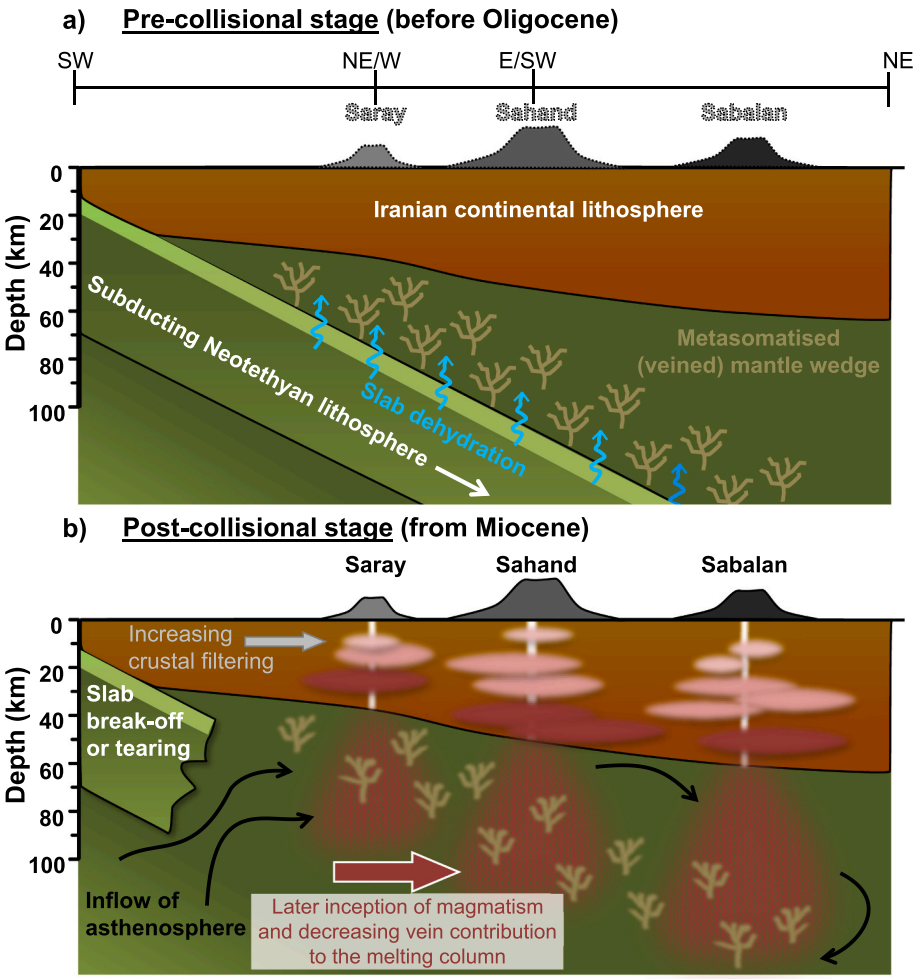


**Fig. 11.** Cartoon showing the proposed conceptual model explaining the time-related progression from the a) pre-collisional to the b) post-collisional stages along the Saray-Sahand-Sabalan array (not to scale). See text for full details.

for of alkali contents, Eu/Eu* and Sr-Nd-Pb isotopes), likely reflecting differences in the source rocks. Indeed, the Bijar-Qorveh adakitic dacites were ascribed to melting of a crustal source mainly consisting of amphibolite-facies metamorphosed gabbroic rocks, with possible contributions from basement metasedimentary lithologies accounting for their strong "crustal" signature (Fedele et al., 2022). In addition, the Bijar-Qorveh dacites show some well-defined differentiation trends but also significant data scattering in numerous variation diagrams (Figs. 5, SM1 and SM2), possibly pointing to the interaction of the evolving melts with crustal lithotypes of variable compositions, consistent with geological evidence. The very coherent differentiation trends observed for Sahand adakitic rocks are instead consistent with differentiation accompanied by limited contamination, in line with the results of the models presented above.

*5.6.2. Local trends in magma compositions*

The composition of the magmas emplaced at Sahand and Sabalan followed different trends in time. In the Sahand case, the Neo-Sahand stage was characterised by less abundant non-adakitic melts with respect to the Paleo-Sahand one. In addition, the adakitic rocks are characterised by a wider compositional variability, reaching strongly evolved rhyolitic compositions. In the Sabalan case, a well-defined progression is instead evident towards a marked increase in the degree of evolution of the magmas. Considering the notable surface extension of both the edifices (> 3000 $km^2$ for Sahand and ~800 $km^2$ for Sabalan) and the large age range of active magmatism (~8 and ~4.5 Myr), it cannot be excluded that the available data for the two volcanoes are not fully representative of the entire activity. Future work aimed at collecting additional stratigraphic, geochronological and petrological data will significantly contribute to clarify many aspects. Nevertheless, some attempts can still be made to interpreting the trends in time for the two volcanoes.

One main factor is likely represented again by crustal filtering, which should have increased in efficiency with time due to the increase of crustal thickness related with the ongoing compressional regime and the emplacement of igneous rocks. This would explain the increased degree of evolution with time that is observed at both volcanoes for the adakitic magmas. In the Sahand case, the concurrent decrease of the emplacement of non-adakitic, mantle derived magmas could be also related to this. However, in the light of the proposed model accounting for the change in magma composition along the Saray-Sahand-Sabalan array, a progressive decline of the triggering thermal pulse can be also hypothesised. The latter, related to the upwelling of sub-lithospheric mantle after the break-off of the subducted slab (Chaharlang et al., 2023; Ghalamghash et al., 2019) or through the propagation of a slab tear, would have caused magmatism to occur at progressively younger ages moving from the Saray to the Sabalan, and would have thus progressively exhausted in the same direction. In the Sahand case, the waning thermal input would have caused not only smaller partial melting degrees of the metasomatised mantle, but possibly also higher vein/peridotite contributions to the magma generation, thus explaining the increase in $K_2O$ and incompatible elements of non-adakitic melts (see Section 5.5). In this context, time-related trends towards K-richer magma compositions at the Saray and decreasing non-adakitic melts

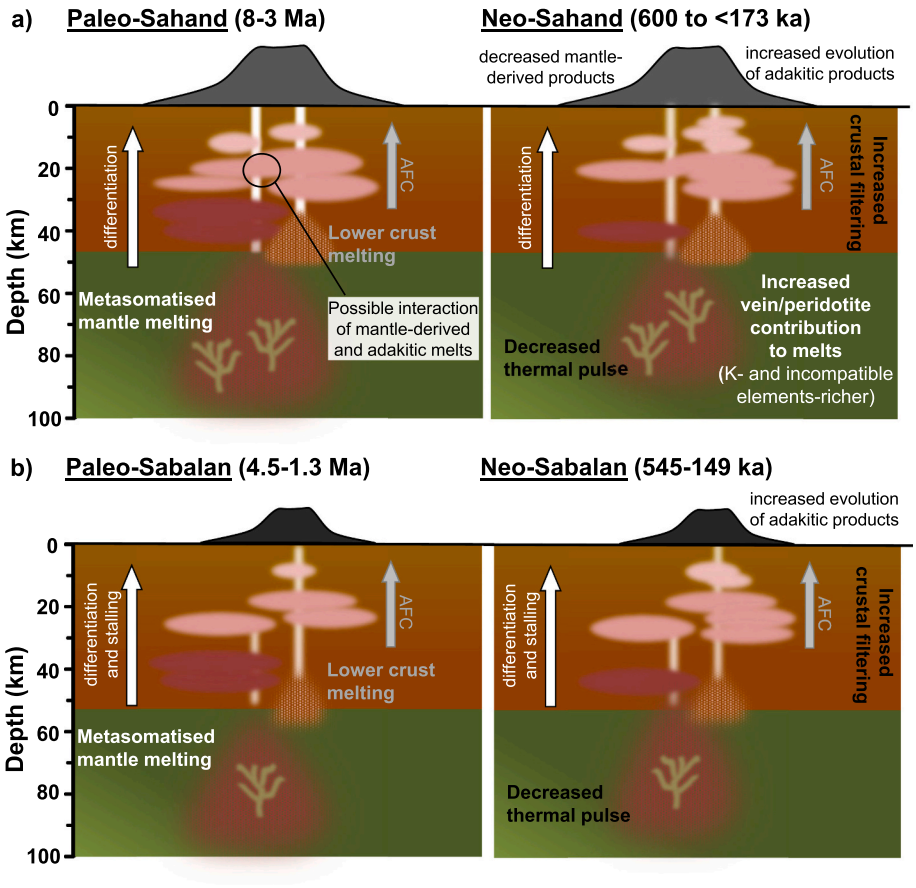


**Fig. 12.** Cartoon showing the proposed conceptual model for the evolution of magmatism at a) Sahand and b) Sabalan volcanoes (not to scale). See text for full details.

production in the Bijar-Qorveh area would be also expected.

## 6. Conclusions

The Miocene-Quaternary igneous activity at the Sahand volcano of NW Iran was characterised by the continuous production of both "normal" calcalkaline, mantle-derived melts, and adakitic, lower-crustal derived melts, emplaced in the context of the Iran-Arabia continental collision. The first were likely generated by the partial melting of lithospheric mantle sources metasomatised during the previous NE-directed subduction of the Neotethyan oceanic lithosphere, and provided the heat necessary to the production of the latter. The two magma types gave rise to two independent liquid lines of descent (although some interaction between the two might have occurred), mainly driven by polybaric closed-system differentiation, accompanied by subordinate interaction with local crustal lithologies.

Comparisons with the style and temporal evolution of magmatism at the coeval neighbouring districts of Saray, Sabalan and Bijar-Qorveh revealed some peculiar trends in both time and space. These are consistent with a model where magmatism is triggered by the upwelling of sub-lithospheric mantle resulting from the break-off of the subducted slab or through the opening of a slab tear. The propagating thermal pulse would account for the progressively later inception of magmatism at increasing distance from the suture zone. The progressive increase in the crustal thickness (and thus of density filtering) observed in the same direction would instead account for the passage from widely variable magmatism, including high-K and near-primitive melts (at Saray), to magmatic activity of paired adakitic and non-adakitic affinity (Sahand), up to adakitic magmatism only (Sabalan). Differences in crustal thickness and composition, coupled with the progressive exhaustion of the thermal pulse, also played a major role on the temporal evolution of the plumbing systems beneath the Sahand and Sabalan volcanoes, where the rock records define a clear trend in time of increasing degree of magma evolution and, in the Sahand case only, decreasing emplacement of non-adakitic magmas.

## Declaration of Competing Interest

The authors declare that they have no known competing financial interests or personal relationships that could have appeared to influence the work reported in this paper.

## Acknowledgements

Rosangela Mauro is thanked for the help in the first stage of preparation of this manuscript. Thanks also to Eleonora Braschi and Andrea Orlando (CNR-IGG, Firenze) and to Marcello Serracino (CNR-IGAG, Roma) for their professionality during the EPMA investigations, and to Domenico Mannetta for high-quality thin section production. Official reviews from Ahmad Rabiee and Fatemeh Sepidbar and careful editorial handling by Co-Editor-in-Chief Di-Cheng Zhu provided fruitful comments and contributed to increase the consistency and readability of the manuscript. This research was granted by PRIN2017 Project 20177BX42Z_005 (Intraplate deformation, magmatism and topographic evolution of a diffuse collisional belt: Insights into the geodynamics of the Arabia-Eurasia collisional zones), funded by MIUR-Italy. Ricerca Dipartimentale DiSTAR (to LF) and Fondi Sapienza Ateneo 2021 and 2022 (ML) grants are also acknowledged.

## Appendix A. Supplementary data

Supplementary data to this article can be found online at https://doi.org/10.1016/j.lithos.2023.107344.

## References


Abbassi, N., Khoshyar, M., Lucas, S.G., Esmaeili, F., 2021. Extensive vertebrate tracksite from the Upper Red Formation (middle-late Miocene), west Zanjan, northwestern Iran. Fossil Rec. 24, 101–116. https://doi.org/10.5194/fr-24-101-2021.

Ahmadzadeh, G., Jahangiri, A., Lentz, D., Mojtahedi, M., 2010. Petrogenesis of Plio-Quaternary post-collisional ultrapotassic volcanism in NW of Marand, NW Iran. J. Asian Earth Sci. 39, 37–50. https://doi.org/10.1016/j.jseaes.2010.02.008.

Aigner-Torres, M., Blundy, J., Ulmer, P., Pettke, T., 2007. Laser Ablation ICPMS study of trace element partitioning between plagioclase and basaltic melts: an experimental approach. Contrib. Mineral. Petrol. 153, 647–667. https://doi.org/10.1007/s00410-006-0168-2.

Alavi, M., 1994. Tectonics of the Zagros orogenic belt of Iran: new data and interpretations. Tectonophysics 229, 211–238.

Allen, M.B., Kheirkhah, M., Neill, I., Emami, M.H., Mcleod, C.L., 2013. Generation of arc and within-plate chemical signatures in collision zone magmatism: quaternary lavas from Kurdistan Province, Iran. J. Petrol. 54, 887–911. https://doi.org/10.1093/petrology/egs090.

Alonso-Perez, R., Müntener, O., Ulmer, P., 2009. Igneous garnet and amphibole fractionation in the roots of island arcs: experimental constraints on andesitic liquids. Contrib. Mineral. Petrol. 157, 541–558. https://doi.org/10.1007/s00410-008-0351-8.

Asiabanha, A., Foden, J., 2012. Post-collisional transition from an extensional volcano-sedimentary basin to a continental arc in the Alborz Ranges, N-Iran. Lithos 148, 98–111. https://doi.org/10.1016/j.lithos.2012.05.014.

Azizi, H., Moinevaziri, H., 2009. Review of the tectonic setting of Cretaceous to Quaternary volcanism in northwestern Iran. J. Geodyn. 47, 167–179. https://doi.org/10.1016/j.jog.2008.12.002.

Azizi, H., Stern, R.J., 2019. Jurassic igneous rocks of the central Sanandaj-Sirjan Zone (Iran) mark a propagating continental rift, not a magmatic arc. Terra Nova 31, 415–432. https://doi.org/10.1111/ter.12404.

Castillo, P.R., 2012. Adakite petrogenesis. Lithos 134-135, 304–316. https://doi.org/10.1016/j.lithos.2011.09.013.

Chaharlang, R., Ghalamghash, J., Saitoh, Y., Ducea, M.N., Schmitt, A.K., 2023. Sr–Nd isotopes of Sabalan Volcano, NW Iran: insights into the origin of collisional adakites and geodynamic implications. Int. J. Earth Sci. https://doi.org/10.1007/s00531-023-02338-x.

Chiaradia, M., Müntener, O., Beate, B., Fontignie, D., 2009. Adakite-like volcanism of Ecuador: lower crust magmatic evolution and recycling. Contrib. Mineral. Petrol. 158, 563–588. https://doi.org/10.1007/s00410-009-0397-2.

Chiu, H.-Y., Chung, S.-L., Zarrinkoub, M.H., Mohammadi, S.S., Khatib, M.M., Iizuka, Y., 2013. Zircon U-Pb age constraints from Iran on the magmatic evolution related to Neotethyan subduction and Zagros orogeny. Lithos 162-163, 70–87. https://doi.org/10.1016/j.lithos.2013.01.006.

Deevsalar, R., Shinjo, R., Ghaderi, M., Murata, M., Hoskin, P.W.O., Oshiro, S., Neill, I., 2017. Mesozoic-Cenozoic mafic magmatism in Sanandaj-Sirjan Zone, Zagros Orogen (Western Iran): geochemical and isotopic inferences from Middle Jurassic and Late Eocene gabbros. Lithos 284, 588–607. https://doi.org/10.1016/j.lithos.2017.05.009.

Delavari, M., Mehrabi, B., Zelenski, M., Chaplygin, I., Nekrylov, N., Shakeri, A., Taran, Y., 2022. The Bazman and Taftan volcanoes of southern Iran: implications for along-arc geochemical variation and magma storage conditions above the Makran low-angle subduction zone. J. Asian Earth Sci. 233, 105259 https://doi.org/10.1016/j.jseaes.2022.105259.

Dostal, J., Zerbi, M., 1978. Geochemistry of Savalan volcano (northwestern Iran). Chem. Geol. 22, 31–42.

Fedele, L., Rahimzadeh, B., Salari, G., Agostini, S., Masoudi, F., Lustrino, M., 2022. A showcase of igneous processes in the Urumieh-Dokhtar Magmatic Arc: the Miocene-Quaternary collisional magmatism of the Bijar-Qorveh area, Northwest Iran. J. Petrol. 63, 1–28 egac047. https://doi.org/10.1093/petrology/egac047.

First, E.C., Hammer, J.E., Ruprecht, P., Rutherford, M., 2021. Experimental constraints on dacite magma storage beneath Volcán Quizapu, Chile. J. Petrol. 62 https://doi.org/10.1093/petrology/egab027 egab027.

Ghalamghash, J., Mousavi, Z., Hassanzadeh, J., Schmitt, A.K., 2016. Geology, zircon geochronology and petrogenesis of Sabalan Volcano: Northwest Iran. J. Volcanol. Geotherm. Res. 327, 192–207. https://doi.org/10.1016/j.jvolgeores.2016.05.001.

Ghalamghash, J., Schmitt, A.K., Chaharlang, R., 2019. Age and compositional evolution of Sahand volcano in the context of post-collisional magmatism in northwestern Iran: evidence for time-transgressive magmatism away from the collisional suture. Lithos 344-345, 265–279. https://doi.org/10.1016/j.lithos.2019.06.031.

Hassanzadeh, J., Wernicke, B.P., 2016. The Neotethyan Sanandaj-Sirjan zone of Iran as an archetype for passive margin-arc transitions. Tectonics 35, 586–621. https://doi.org/10.1002/2015TC003926.

Hastie, A.R., Kerr, A.C., Pearce, J.A., Mitchell, S.F., 2007. Classification of altered volcanic island arc rocks using immobile trace elements: development of the Th-Co discrimination diagram. J. Petrol. 48, 2341–2357. https://doi.org/10.1093/petrology/egm062.

Hunziker, D., Burg, J.P., Bouilhol, P., Quadt, A., 2015. Jurassic rifting at the Eurasian Tethys margin: geochemical and geochronological constraints from granitoids of North Makran, southeastern Iran. Tectonics 34, 571–593. https://doi.org/10.1002/2014TC003768.

Jagoutz, O., Burg, J.P., Hussain, S., Dawood, H., Pettke, T., Lizuka, T., Maruyama, S., 2009. Construction of the granitoid crust of an island arc part I: geochronological and geochemical constraints from the plutonic Kohistan (NW Pakistan). Contrib. Mineral. Petrol. 158, 739–755. https://doi.org/10.1007/s00410-009-0408-3.

Jahangiri, A., 2007. Post-collisional Miocene adakitic volcanism in NW Iran: geochemical and geodynamic implications. J. Asian Earth Sci. 30, 433–447. https://doi.org/10.1016/j.jseaes.2006.11.008.

Kheirkhah, M., Allen, M.B., Emami, M., 2009. Quaternary syn-collision magmatism from the Iran/Turkey borderlands. J. Volcanol. Geotherm. Res. 182, 1–12. https://doi.org/10.1016/j.jvolgeores.2009.01.026.

King, A.J., Philips, K.J.H., Vita-Finzi, C., Russell, S.S., 2020. Terrestrial modification of the Ivuna meteorite and a reassessment of the chemical composition of the CI type specimen. Geochim. Cosmochim. Acta 268, 73–89. https://doi.org/10.1016/j.gca.2019.09.041.

Kolb, M., Von Quadt, A., Peytcheva, I., Heinrich, C.A., Fowler, S.J., Cvetković, V., 2013. Adakite-like and normal arc magmas: distinct fractionation paths in the East Serbian segment of the Balkan-Carpathian Arc. J. Petrol. 54, 421–451. https://doi.org/10.1093/petrology/egs072.

Laubier, M., Grove, T.L., Langmuir, C.H., 2014. Trace element mineral/melt partitioning for basaltic and basaltic andesitic melts: an experimental and laser ICP-MS study with application to the oxidation state of mantle source regions. Earth Planet. Sci. Lett. 392, 265–278. https://doi.org/10.1016/j.epsl.2014.01.053.

Le Maitre, R.W., 2002. Igneous Rocks: A Classification and Glossary of Terms. Recommendations of the International Union of Geological Sciences Subcommission on the Systematics of Igneous Rocks. Cambridge University Press, Cambridge, UK, 256 pp.

Lechmann, A., Burg, J.P., Ulmer, P., Guillong, M., Faridi, M., 2018. Metasomatized mantle as the source of Mid-Miocene-Quaternary volcanism in NW-Iranian Azerbaijan: geochronological and geochemical evidence. Lithos 304-307, 311–328. https://doi.org/10.1016/j.lithos.2018.01.030.

Luffi, P., Ducea, M.N., 2022. Chemical mohometry: assessing crustal thickness of ancient orogens using geochemical and isotopic data. Rev. Geophys. 60 https://doi.org/10.1029/2021RG000753 e2021RG000753.

Lustrino, M., Anderson, D.L., 2015. The mantle isotopic printer: Basic mantle plume geochemistry for seismologists and geodynamicists. In: Foulger, G.R., Lustrino, M., King, S.D. (Eds.), The Interdisciplinary Earth: a Volume in honor of Don L. Anderson, Geological Society of America Special Paper 514 and American Geophysical Union Special Publication, 71, pp. 257–279. https://doi.org/10.1130/2015.2514(16).

Lustrino, M., Duggen, S., Rosenberg, C., 2011. The Central-Western Mediterranean: anomalous igneous activity in an anomalous collisional tectonic setting. Earth Sci. Rev. 104, 1–40. https://doi.org/10.1016/j.earscirev.2010.08.002.

Lustrino, M., Keskin, M., Mattioli, M., Kavak, O., 2012. Heterogeneous mantle sources feeding the volcanic activity of Mt. Karacadağ (SE Turkey). J. Asian Earth Sci. 46, 120–139. https://doi.org/10.1016/j.jseaes.2011.11.016.

Lustrino, M., Fedele, L., Agostini, S., Prelević, D., Salari, G., 2019. Leucitites within and around the Mediterranean area. Lithos 324-325, 216–233. https://doi.org/10.1016/j.lithos.2018.11.007.

Lustrino, M., Salari, G., Rahimzadeh, B., Fedele, L., Masoudi, F., Agostini, S., 2021. Quaternary melanephelinites and melilitites from Nowbaran (NW Urumieh-Dokhtar Magmatic Arc, Iran): origin of ultrabasic-ultracalcic melts in a post-collisional setting. J. Petrol. 62, 1–31. https://doi.org/10.1093/petrology/egab058.

Lyubetskaya, T., Korenaga, J., 2007. Chemical composition of Earth's primitive mantle and its variance: 1. Methods and results. J. Geophys. Res. 112, B03211. https://doi.org/10.1029/2005JB004223.

Macpherson, C., Dreher, S.T., Thirlwall, M., 2006. Adakites without slab melting: High pressure differentiation of island arc magma, Mindanao, the Philippines. Earth Planet. Sci. Lett. 243, 581–593. https://doi.org/10.1016/j.epsl.2005.12.034.

Marchev, P., Georgiev, S., Raicheva, R., Peytcheva, I., von Quadt, A., Ovtcharova, M., Bonev, N., 2013. Adakitic magmatism in post-collisional setting: an example from the early-middle Eocene magmatic belt in Southern Bulgaria and Northern Greece. Lithos 180-181, 159–180. https://doi.org/10.1016/j.lithos.2013.08.024.

McQuarrie, N., van Hinsbergen, D.J., 2013. Retrodeforming the Arabia-Eurasia collision zone: age of collision versus magnitude of continental subduction. J. Geol. 41, 315–318. https://doi.org/10.1130/G33591.1.

Mehdipour Ghazi, J., Moazzen, M., 2015. Geodynamic evolution of the Sanandaj-Sirjan Zone, Zagros Orogen, Iran, Turkish. J. Earth Sci. 24, 513–528. https://doi.org/10.3906/yer-1404-12.

Moayyed, M., Moazzen, M., Calagari, A.A., Jahangiri, A., Modjarrad, M., 2008. Geochemistry and petrogenesis of lamprophyric dykes and the associated rocks from Eslamy peninsula, NW Iran: implications for deep-mantle metasomatism. Chem. Erde-Geochem. 68, 141–154. https://doi.org/10.1016/j.chemer.2006.04.002.

Moghadam, H.S., Ghorbani, G., Khedr, M.Z., Fazlnia, N., Chiaradia, M., Eyuboglu, Y., Santosh, M., Francisco, C.G., Martinez, M.L., Gourgaud, A., Arai, S., 2014. Late Miocene K-rich volcanism in the Eslamieh Peninsula (Saray), NW Iran: implications for geodynamic evolution of the Turkish–Iranian High Plateau. Gondwana Res. 26, 1028–1050. https://doi.org/10.1016/j.gr.2013.09.015.

Moghadam, H.S., Griffin, W.L., Kirchenbaur, M., Garbe-Schönberg, D., Khedr, M.Z., Kimura, J.-I., Stern, R.J., Ghorbani, G., Murphy, R., O'Reilly, S.Y., Arai, S., Maghdour-Mashhour, R., 2018. Roll-Back, extension and mantle upwelling triggered Eocene potassic magmatism in NW Iran. J. Petrol. 59, 1417–1465. https://doi.org/10.1093/petrology/egy067.

Moine Vaziri, H., Amine Sobhani, E., 1977. Carte Geologique du Sahand 1:100,000 (Ecole normale superieure de Tehran).

Moyen, J.-F., 2009. High Sr/Y and La/Yb: the meaning of the "adakitic signature". Lithos 112, 556–574. https://doi.org/10.1016/j.lithos.2009.04.001.
Muttoni, G., Mattei, M., Balini, M., Zanchi, A., Gaetani, M., Berra, F., 2009. The drift history of Iran from the Ordovician to the Triassic. In: Brunet, M.-F., Wilmsen, M., Granath, J.W. (Eds.), South Caspian to Central Iran Basins, Geological Society of London Special Publication, vol. 312, pp. 7–29. https://doi.org/10.1144/SP312.2.
Nandedkar, R.H., Hürlimann, N., Ulmer, P., Müntener, O., 2016. Amphibole-melt trace element partitioning of fractionating calcalkaline magmas in the lower crust: an experimental study. Contrib. Mineral. Petrol. 171, 71. https://doi.org/10.1007/s00410-016-1278-0.
Neill, I., Meliksetian, K., Allen, M.B., Navasardyan, G., Kuiper, K., 2015. Petrogenesis of mafic collision zone magmatism: the Armenian sector of the Turkish-Iranian Plateau. Chem. Geol. 403, 24–41. https://doi.org/10.1016/j.chemgeo.2015.03.013.
Omrani, J., Agard, P., Whitechurch, H., Benoit, M., Prouteau, G., Jolivet, L., 2008. Arc-magmatism and subduction history beneath the Zagros Mountains, Iran: a new report of adakites and geodynamic consequences. Lithos 106, 380–398. https://doi.org/10.1016/j.lithos.2008.09.008.
Pang, K.-N., Chung, S.-L., Zarrinkoub, M.H., Khatib, M.M., Mohammadi, S.S., Chiu, H.-Y., Chu, C.-H., Lee, H.-Y., Lo, C.-H., 2013a. Eocene-Oligocene post-collisional magmatism in the Lut-Sistan region, eastern Iran: magma genesis and tectonic implications. Lithos 180-181, 234–251. https://doi.org/10.1016/j.lithos.2013.05.009.
Pang, K.-N., Chung, S.-L., Zarrinkoub, M.H., Lin, Y.-C., Lee, H.-Y., Lo, C.-H., Khatib, M. M., 2013b. Iranian ultrapotassic volcanism at ~11 Ma signifies the initiation of post-collisional magmatism in the Arabia-Eurasia collision zone. Terra Nova 25, 405–413. https://doi.org/10.1111/ter.12050.
Pang, K.-N., Chung, S.-L., Zarrinkoub, M.H., Li, X.-H., Lee, H.-Y., Lin, T.-H., Chiu, H.-Y., 2016. New age and geochemical constraints on the origin of Quaternary adakite-like lavas in the Arabia-Eurasia collision zone. Lithos 264, 348–359. https://doi.org/10.1016/j.lithos.2016.08.042.
Pearce, J.A., 1996. A user's guide to basalt discrimination diagrams. In: Wyman, D.A. (Ed.), Trace Element Geochemistry of Volcanic Rocks: Application for Massive Sulphide Exploration, Geological Association of Canada, Short Course Notes, vol. 12, pp. 79–113.
Peccerillo, A., 2017. Cenozoic Volcanism in the Tyrrhenian Sea Region. Advances in Volcanology, Springer Cham. https://doi.org/10.1007/978-3-319-42491-0, 399 pp.
Pertermann, M., Hirschmann, M.M., Hametner, K., Günther, D., Schmidt, M.W., 2004. Experimental determination of trace element partitioning between garnet and silica-rich liquid during anhydrous partial melting of MORB-like eclogite. Geochem. Geophys. Geosyst. 5, Q05A01. https://doi.org/10.1029/2003GC000638.
Pirmohammadi Alishah, F., Jahangiri, A., 2013. Post-collisional pliocene to pleistocene adakitic volcanism in Sahand region in Northwest Iran: Geochemical and geodynamic implications. Physical Sciences Research International 1, 62–75.
Plank, T., 2014. The chemical composition of subducting sediments. In: Holland, H.D., Turekian, K.K. (Eds.), Treatise on Geochemistry, 2nd ed. Elsevier, Amsterdam, pp. 607–629. https://doi.org/10.1016/B978-0-08-095975-7.00319-3. 4, The Crust.
Priestley, K., McKenzie, D., Barron, J., Tatar, M., Debayle, E., 2012. The Zagros core: deformation of the continental lithospheric mantle. Geochem. Geophys. Geosyst. 13, Q11014. https://doi.org/10.1029/2012GC004435.
Prouteau, G., Scaillet, B., 2003. Experimental constraints on the origin of the 1991 Pinatubo dacite. J. Petrol. 44, 2203–2241. https://doi.org/10.1093/petrology/egg075.
Qian, Q., Hermann, J., 2013. Partial melting of lower crust at 10-15 kbar: constraints on adakite and TTG formation. Contrib. Mineral. Petrol. 165, 1195–1224. https://doi.org/10.1007/s00410-013-0854-9.
Rabiee, A., Rossetti, F., Asahara, Y., Azizi, H., Lucci, F., Lustrino, M., Noazem, R., 2020. Long-lived, Eocene-Miocene stationary magmatism in NW Iran along a transform plate boundary. Gondwana Res. 85, 237–262. https://doi.org/10.1016/j.gr.2020.03.014.
Rabiee, A., Rossetti, F., Lucci, F., Lustrino, M., 2022. Cenozoic porphyry and other hydrothermal ore deposits along the South Caucasus-West Iranian tectono-magmatic belt: a critical reappraisal of the controlling factors. Lithos 430-431, 106874. https://doi.org/10.1016/j.lithos.2022.106874.
Rahimzadeh, B., Mahmoudi, S., Corfu, F., Ahadnajad, V., Von Quadt, A., 2021. A unique period of bimodal volcanism at 130-110 Ma in the northern Sanandaj-Sirjan Zone: evidence for an extensional setting. Lithos 392–393, 106155. https://doi.org/10.1016/j.lithos.2021.106155.
Reichenbacher, B., Alimohammadian, H., Sabouri, J., Haghfarshi, E., Faridi, M., Abbasi, S., Matzke-Karasz, R., Fellin, M.G., Carnevale, G., Schiller, W., Vasilyan, D., Scharrer, S., 2011. Late Miocene stratigraphy, palaeoecology and palaeogeography of the Tabriz Basin (NW Iran, Eastern Paratethys). Palaeogeogr. Palaeoclimatol. Palaeoecol. 311, 1–18. https://doi.org/10.1016/j.palaeo.2011.07.009.
Ribeiro, J.M., Maury, R.C., Grégoire, M., 2016. Are adakites slab melts or high-pressure fractionated mantle melts? J. Petrol. 57, 839–862. https://doi.org/10.1093/petrology/egw023.
Richards, J.P., Kerrich, R., 2007. Special paper: Adakite-like rocks: their diverse origins and questionable role in metallogenesis. Econ. Geol. 102, 537–576. https://doi.org/10.2113/gsecongeo.102.4.537.
Ridolfi, F., Renzulli, A., Puerini, M., 2010. Stability and chemical equilibrium of amphibole in calc-alkaline magmas: an overview, new thermobarometric formulations and application to subduction-related volcanoes. Contrib. Mineral. Petrol. 160, 45–66. https://doi.org/10.1007/s00410-009-0465-7.
Rodríguez, C., Sellés, D., Dungan, M., Langmuir, C., Leeman, W., 2007. Adakitic dacites formed by intracrustal crystal fractionation of water-rich parent magmas at Nevado de Longaví Volcano (36.2°S; Andean Southern Volcanic Zone, Central Chile). J. Petrol. 48, 2033–2061. https://doi.org/10.1093/petrology/egm049.
Salari, G., Lustrino, M., Ghorbani, M.R., Agostini, S., Fedele, L., 2021. Petrological characterization of the Cenozoic igneous rocks of the Tafresh area, central Urumieh-Dokhtar Magmatic Arc (Iran). Periodico di Mineralogia 90, 59–83. https://doi.org/10.13133/2239-1002/16620.
Sawada, Y., Zaree, G.R., Sakai, T., Itaya, T., Yagi, K., Imaizumi, M., Mirzaie-Ataabadi, M., Fortelius, M., 2016. K-Ar ages and petrology of the late Miocene pumices from the Maragheh Formation, northwest Iran. Palaeobiodiversity and Palaeoenvironments 96, 399–431. https://doi.org/10.1007/s12549-016-0232-5.
Şengör, A.M.C., Altiner, D., Zabci, C., Sunal, G., Lom, N., Aylan, E., Öner, T., 2023. On the nature of the Cimmerian Continent. Earth Sci. Rev. 104520 https://doi.org/10.1016/j.earscirev.2023.104520.
Shafaii Moghadam, H., Li, Q.L., Griffin, W.L., Stern, R.J., Ishizuka, O., Henry, H., Lucci, F., O'Reilly, S.Y., Ghorbani, G., 2020. Repeated magmatic buildup and deep "hot zones" in continental evolution: the Cadomian crust of Iran. Earth Planet. Sci. Lett. 531, 115989 https://doi.org/10.1016/j.epsl.2019.115989.
Song, S., Niu, Y., Su, L., Wei, C., Zhang, L., 2014. Adakitic (tonalitic-trondhjemitic) magmas resulting from eclogite decompression and dehydration melting during exhumation in response to continental collision. Geochim. Cosmochim. Acta 130, 42–62. https://doi.org/10.1016/j.gca.2014.01.008.
Stern, R.J., Moghadam, H.S., Pirouz, M., Mooney, W., 2021. The geodynamic evolution of Iran. Annu. Rev. Earth Planet. Sci. 49, 9–36. https://doi.org/10.1146/annurev-earth-071620-052109.
Swisher, C.C., 1996. New $^{40}Ar/^{39}Ar$ dates and their contribution toward a revised chronology for the late Miocene of Europe and West Asia. In: Bernor, R.L., Fahlbusch, V., Mittmann, H.W. (Eds.), The Evolution of Western Eurasian Neogene Mammal Faunas. Columbia University Press, New York, pp. 64–77.
Tang, G.-J., Wang, Q., Wyman, D.A., Chung, S.-L., Chen, H.-Y., Zhao, Z.-H., 2017. Genesis of pristine adakitic magmas by lower crustal melting: a perspective from amphibole composition. J. Geophys. Res. Solid Earth 122, 1934–1948. https://doi.org/10.1002/2016JB013678.
van Hinsbergen, D.J.J., Torsvik, T.H., Schmid, S.M., Matenco, L.C., Maffione, M., Vissers, R.L.M., Gurer, D., Spakman, W., 2020. Orogenic architecture of the Mediterranean region and kinematic reconstructions of its tectonic evolution since the Triassic. Gondwana Res. 81, 79–229. https://doi.org/10.1016/j.gr.2019.07.009.
Verdel, C., Wernicke, B.P., Hassanzadeh, J., Guest, B., 2011. A Paleogene extensional arc flare-up in Iran. Tectonics 30, TC3008. https://doi.org/10.1029/2010TC002809.
Wang, J., Dan, W., Wang, Q., Tang, G.-J., 2021. High-Mg# adakitic rocks formed by lower-crustal magma differentiation: mineralogical and geochemical evidence from garnet-bearing diorite porphyries in Central Tibet. J. Petrol. 62 https://doi.org/10.1093/petrology/egaa099 egaa099.